Alexander Eber, BSc

Measurements of normal spectral emissivity data @684.5 nm of metals in the solid and liquid phase using a μs-DOAP

MASTER'S THESIS

to achieve the university degree of

Diplom-Ingenieur

Master's degree programme: Technical Physics

submitted to

Graz University of Technology

Supervisor

Gernot Pottlacher, Ao.Univ.-Prof. Dipl-Ing. Dr.techn.

Institute of Experimental Physics

Co-Supervisor: Peter Pichler, Dipl.-Ing. BSc

Institute of Experimental Physics

Graz, December 2020

AFFIDAVIT

I declare that I have authored this thesis independently, that I have not used other than the declared sources/resources, and that I have explicitly indicated all material which has been quoted either literally or by content from the sources used. The text document uploaded to TUGRAZonline is identical to the present master's thesis.

Date, Signature

Acknowledgement

First and foremost, I want to thank *Prof. Gernot Pottlacher* for the excellent guidance and supervision throughout the entire duration of this master thesis. He made it possible for me to write this thesis at the Thermo- and Metalphysics Group, get a better understanding of scientific research and to write a publication about my findings. Secondly, I wish to show special gratitude to my co-supervisor *DI Peter Pichler*, who taught me the ins and outs of the ohmic pulse heating apparatus and the μs-DOAP and helped me to overcome countless experimental challenges. Additionally, I wish to thank the members of the working group *DI Thomas Leitner* and *Dr. Matthias Leitner* for countless discussions and inputs. I really enjoyed working with you and being part of this amazing team for the past months.

Special gratitude goes to all proof-readers of this thesis for their thoroughness, especially my sister *Teresa*, who read through the entire thesis and came up with numerous very helpful suggestions.

Finally, I want to thank my parents because all of this would not have been possible without their unconditional guidance, support and love.

Abstract

In this thesis, normal spectral emissivity data are measured for four different high melting metals. The ohmic pulse-heating apparatus is used to measure temperature dependent properties. The sample is heated, using their own ohmic resistances by applying a high voltage across the wire-shaped sample. The sample is heated through the solid phase, towards the melting point and then throughout the liquid phase, until the sample explodes at the boiling point.

Tantalum, niobium, molybdenum and tungsten data were evaluated separately in the solid and the liquid phase. Although these materials were already measured in the *Thermophysics and Metalphysics* group at *Graz University of Technology* and data were published in the liquid phase, data of the solid phase were unreliable because of inconsistent surface preparations.

However, before any measurements could be performed, a calibration was done in order to determine the device matrix and then the measurement positions needed to be adjusted.

The results in the liquid phase matched the previous results for tantalum, niobium and tungsten. For molybdenum, a deviation of about 20 % from previous data, published for example in 2004, *Cagran et al.* [1] was determined. A re-evaluation of the previously measured data was performed and after some modifications, the results match the newly measured data.

Additionally, a comprehensive uncertainty evaluation according to *Guide to the expression of uncertainty in measurement* (GUM) [2] was performed. This included several different factors of the apparatus itself and the statistical deviation of the different experiments. The results show, that the statistical deviation is by far the more dominant uncertainty to consider.

Kurzfassung

Diese Arbeit beschäftigt sich mit der Messung des normalen spektralen Emissionskoeffizienten für vier verschiedene Metalle mit hoher Schmelztemperatur. Für die Messung temperaturabhängiger Eigenschaften ist eine ohmsche Pulsheizvorrichtung in Verwendung. Die Probe wird durch ihren eigenen ohmschen Widerstand unter Anlegen einer Hochspannung an die drahtförmige Probe erhitzt. Dabei wird sie durch die feste Phase zum Schmelzpunkt und dann durch die flüssige Phase erhitzt, bis die Probe schlussendlich explodiert, sobald sie den Siedepunkt erreicht.

Die Elemente Tantal, Niob, Molybdän und Wolfram wurden vermessen und die feste und die flüssige Phase wurden voneinander getrennt ausgewertet. Obwohl diese Materialien bereits in der Arbeitsgruppe *Thermophysik and Metallphysik* an der *Technischen Universität Graz* vermessen wurden, waren Daten der festen Phase aufgrund inkonsistenter Oberflächenvorbereitungen unzuverlässig.

Die Ergebnisse in der flüssigen Phase stimmen mit den vorherigen Ergebnissen für Tantal, Niob und Wolfram überein. Für Molybdän wurde eine Abweichung von etwa 20 % im Vergleich zu früheren Daten, die beispielsweise in 2004, *Cagran et al.* [1] veröffentlicht wurden, berechnet. Eine erneute Auswertung der zuvor gemessenen Daten wurde durchgeführt und nach einigen Adaptierungen stimmen die Ergebnisse mit den neu gemessenen Daten überein.

Zusätzlich wurde eine umfassende Unsicherheitsberechnung nach dem *Guide to the expression of uncertainty in measurement* (GUM) [2] durchgeführt. Diese Berechnung umfasst verschiedene Faktoren der Vorrichtung. Zusätzlich wird die statistische Abweichung der verschiedenen Experimente miteinbezogen. Die Ergebnisse zeigen, dass die statistische Abweichung bei weitem die dominierende Unsicherheit ist.

Abbreviations and Physical quantities

Physical Constants

h	=	$6.62607015 \cdot 10^{-34}$ J $\cdot$ s	[3]	... universal Planck constant
k_B	=	$1.380649 \cdot 10^{-23}$ J $\cdot$ K^{-1}	[3]	... universal Boltzmann constant
c_0	=	299792458 m $\cdot$ s^{-1}	[3]	... speed of light in vacuum
σ	=	$5.670 \cdot 10^{-8}$ W $\cdot$ m^{-2} $\cdot$ K^{-4}	[4]	... Stephan-Boltzmann constant
c_1	=	$3.741832 \cdot 10^{-16}$ W $\cdot$ m^2	[5]	... first radiation constant
c_2	=	$1.43879 \cdot 10^{-2}$ m $\cdot$ K	[5]	... second radiation constant

Abbreviations

OPA	...	ohmic pulse-heating apparatus
(μs -) DOAP	...	microsecond division of amplitude photopolarimeter
PSG	...	polarization state generator
PSD	...	polarization state detector

List of symbols

T	...	absolute temperature	/	K
T_{rad}	...	radiance temperature	/	K
t	...	time	/	s
λ	...	wavelength	/	m
Φ	...	radiant flux	/	W
Q	...	emitted energy	/	J
θ'	...	zenith angle	/	rad
ϕ'	...	azimuth angle	/	rad
A	...	area of emitting surface	/	m^2
ω	...	solid angle	/	sr
L	...	radiance	/	$\text{W} \cdot \text{m}^{-3} \cdot \text{sr}^{-1}$
M	...	self-exitance	/	$\text{W} \cdot \text{m}^{-2}$
Z	...	voltage	/	V
I_{0-3}	...	intensity	/	W/m^2
S_{1-4}	...	Stokes parameter	/	W/m^2
Δ	...	ellipsometry angle or parameter	/	rad
ψ	...	ellipsometry angle or parameter	/	rad
K	...	calibration constant of the pyrometer	/	V
ϵ	...	emissivity		
$(deg)P$	...	degree of polarization		
a	...	main axis of polarisation ellipsis		
b	...	minor axis of polarisation ellipsis		
n	...	index of refraction		
k	...	extinction coefficient		
$\overleftrightarrow{A}$	...	device matrix		

Contents

List of Figures

List of Tables

1 Motivation

In the *Thermophysics and Metalphysics* group at *Institute of Experimental Physics* at the *Graz University of Technology*, a fast ohmic pulse-heating apparatus (OPA) has been used since 1979, to measure temperature dependent thermophysical properties. The measurement process starts at room temperature, goes on through the solid and the liquid phase and ends once the boiling point of the material is reached and the wire explodes. Typically, the experiment is finished after about 40 µs and several thousand Kelvin are reached.

Liquid metals react easily with any other material. Therefore, contactless measurements are needed. The International Temperature Scale of 1990 (ITS-90) [6] defines temperature above the melting point of silver (1234.93 K) by spectral pyrometry. An especially designed pyrometer, for very fast time responses, is used to measure the radiance temperature of the wire. To calculate the real temperature from the radiance temperature, the emissivity is needed.

Since 2000, additionally a microsecond Division of Amplitude Photopolarimeter (µs-DOAP) is used in this measurement apparatus. It allows the determination of the normal spectral emissivity at the wavelength of the laser used, 684.5 nm, as a function of time. In combination with the pyrometer and its measured radiance temperature time dependence, the normal spectral emissivity as a function of radiance temperature can be calculated. The µs-DOAP used, is a special photopolarimeter, to measure a reasonable number of data points during the short experiment time. The polarimeter used, was described by 1982, *Azzam* [7] and works without any moving or rotating parts, which is why it provides a high temporal resolution.

In this thesis, the µs-DOAP is used to measure the normal spectral emissivity for four different pure metals. The high melting temperature metals

tantalum (Ta), niobium (Nb), molybdenum (Mo) and tungsten (W) were examined for their emissivity. For the evaluations, the solid and the liquid phase are treated separately. Afterwards the data points are compared with data from different publications.

During the calibration process of the μs-DOAP, different setup-specific dependences on the uncertainty were examined. These dependences are later used for an uncertainty calculation according to the *Guide to the expression of uncertainty in measurement* (GUM). Additionally, the statistical uncertainty of single measurements is added to the setup-specific uncertainty for the calculation of a combined uncertainty of the normal spectral emissivity.

2 Introduction to radiation of a surface

In this chapter, the main concepts of radiation from an emitting surface are explained, starting with a geometric description of emission from a surface. A closer look is taken at a black body with its ideal properties of emission and absorption. Then the concept of emissivity is explained in detail because it is the main parameter measured in this thesis. Special focus is put on different descriptor types for the emissivity, their definitions and their relations to other types of emissivity.

2.1 Terminology and Definitions

The first important definition is the *radiant flux* Φ_{em} (in W). It describes the power, which is emitted from the radiating surface. It is calculated with the derivative of the emitted energy Q with respect to time t. [8]

$$\Phi_{em} = \frac{dQ}{dt} \tag{2.1}$$

The *spectral radiant power* $\Phi_{\lambda,em}$ (in W/m) is used, if only a certain wavelength λ is considered. It is defined as the derivative of the radiant flux with respect to the wavelength [1].

$$\Phi_{\lambda,em} = \frac{d\Phi_{em}}{d\lambda} \tag{2.2}$$

[1] This chapter, unless marked otherwise, follows Chapter 1.2 from 1989, *DeWitt and Nutter* [9].

For a real surface, the emitted radiation is usually dependent on the direction. The physical quantity radiance L considers this dependence. The direction is usually specified in a spherical coordinate system with the pair of a zenith θ' and an azimuth ϕ' angle. The zenith angle defines the angle between the normal of the emitting surface $\mathrm{d}A$ and the direction of the light. [10] This geometric description is shown in Figure 2.1. A small surface area in space $\mathrm{d}A'_\mathrm{n}$, with a distance r to the emitting surface, which is normal to the (θ', ϕ') direction, defines a small solid angle $\mathrm{d}\omega'$ according to Equation 2.3.

$$\mathrm{d}\omega' = \frac{\mathrm{d}A'_\mathrm{n}}{r^2} \tag{2.3}$$

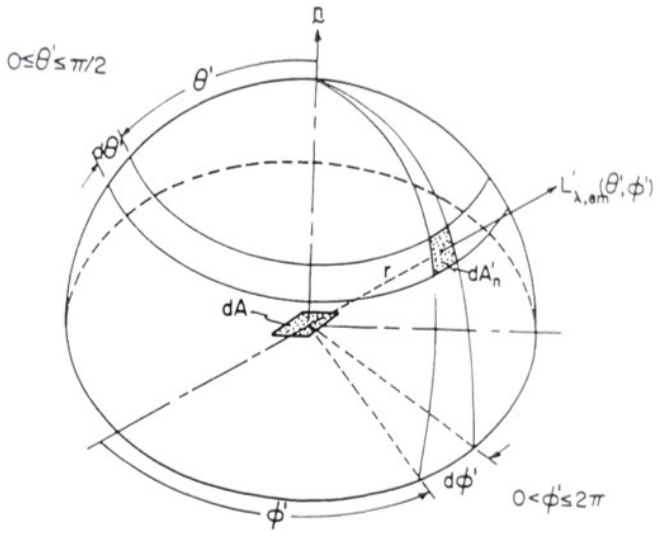

Figure 2.1: Geometric description of the solid angle $\mathrm{d}\omega'$ using a spherical coordinate system with a zenith θ' and an azimuth ϕ' angle, Figure 1.9 from 1989, *DeWitt and Nutter* [9].

A differential part of a spherical surface in a spherical coordinate system is given by

$$\mathrm{d}A'_\mathrm{n} = r^2 \cdot sin(\theta') \cdot \mathrm{d}\theta' \cdot \mathrm{d}\phi' \tag{2.4}$$

and therefore, the differential solid angle can also be written as

$$\mathrm{d}\omega' = sin(\theta') \cdot \mathrm{d}\theta' \cdot \mathrm{d}\phi'. \tag{2.5}$$

The *spectral radiance* $L'_{\lambda,\mathrm{em}}$ (in $\mathrm{W{\cdot}m^{-2}\cdot sr^{-1}}$) describes the rate of emission from $\mathrm{d}A$ through $\mathrm{d}A'_{\mathrm{n}}$, if the radiation is emitted from a differential surface $\mathrm{d}A$ in the centre of the coordinate system. In many cases the radiance is only calculated for a certain wavelength λ, which is then called spectral radiance.

$$L'_{\lambda,\mathrm{em}}(\lambda,\theta',\phi') = \frac{\mathrm{d}^3\Phi'_{\mathrm{em}}}{\mathrm{d}A\cdot cos(\theta')\cdot \mathrm{d}\omega'\cdot \mathrm{d}\lambda} \tag{2.6}$$

Using Equation 2.2, the spectral radiance can also be written in dependence of the spectral radiance power.

$$L'_{\lambda,\mathrm{em}}(\lambda,\theta',\phi') = \frac{\mathrm{d}^2\Phi'_{\lambda,\mathrm{em}}}{\mathrm{d}A\cdot cos(\theta')\cdot \mathrm{d}\omega'} \tag{2.7}$$

Another important quantity is the *spectral self-exitance* $M_{\lambda,\mathrm{em}}$. It describes the spectral radiant flux, which is emitted by the surface, per unit area of the radiating surface.

$$M_{\lambda,\mathrm{em}}(\lambda) = \frac{\mathrm{d}\Phi'_{\lambda,\mathrm{em}}}{\mathrm{d}A} = \int_0^{2\pi}\int_0^{\pi/2} L'_{\lambda,\mathrm{em}}(\lambda,\theta',\phi')\cdot cos(\theta')\cdot sin(\theta')\mathrm{d}\theta'\mathrm{d}\phi' \tag{2.8}$$

By integrating Equation 2.8 over all wavelengths, the total radiant power per unit area or *total self-exitance* M_{em} can be calculated.

$$M_{\mathrm{em}} = \int_0^{\infty} M_{\lambda,\mathrm{em}}(\lambda)\mathrm{d}\lambda \tag{2.9}$$

2.2 Radiation of a Black Body

A black body describes an ideal surface, which can describe an ideal thermal emitter or absorber. An ideal absorber absorbs all radiation hitting the surface, independent of wavelength or direction. As an ideal emitter, a black body emits, for a certain wavelength and temperature, more radiation than any real body. Additionally, the emitted radiation of a black body is independent of direction. This direction independence describes a diffuse

emitter. Many radiative properties of real surfaces use a black body as reference because of the ideal properties as an absorber or emitter. [8, 9]

Planck's law (Equation 2.10) describes the relation between the spectral radiance of a black body $L_{\lambda,\mathrm{b}}$, the wavelength of the radiation λ and the temperature T with the help of two constants c_1 and c_2. [8]

$$L_{\lambda,\mathrm{b}} = \frac{c_1}{\lambda^5} \cdot \left(e^{\frac{c_2}{\lambda \cdot T}} - 1 \right)^{-1} \tag{2.10}$$

c_1 and c_2 can be calculated purely from natural constants with Equation 2.11 and Equation 2.12. [8]

$$c_1 = 2 \cdot h \cdot c_0^2 \tag{2.11}$$

$$c_1 = \frac{h \cdot c_0}{k_B} \tag{2.12}$$

h ... Planck's quantum of action / J · s
c_0 ... speed of light in vacuum / m·s^{-1}
k_B ... Boltzmann constant / m^2 · kg · s^{-2} · K^{-1}

In Figure 2.2 the spectral radiance of a black body is demonstrated for some selected temperatures. The maximum of the spectral radiance moves towards shorter wavelengths at higher temperatures because a higher energy is contained. Additionally the value of the spectral radiance increases for higher temperatures at every wavelength. The sun can be estimated as a black body with a temperature of 5800 K [9]. For comparison, the visible range is marked with two vertical dotted lines (400 nm and 700 nm) [11]. The maximum of the 5800 K distribution is right in the visible area but there is also a substantial part at even higher wavelengths, specifically in the infrared region.

The total radiance of a black body can be calculated by integrating the spectral radiance over all possible wavelengths. The result is the Stephan-Boltzmann law. [9]

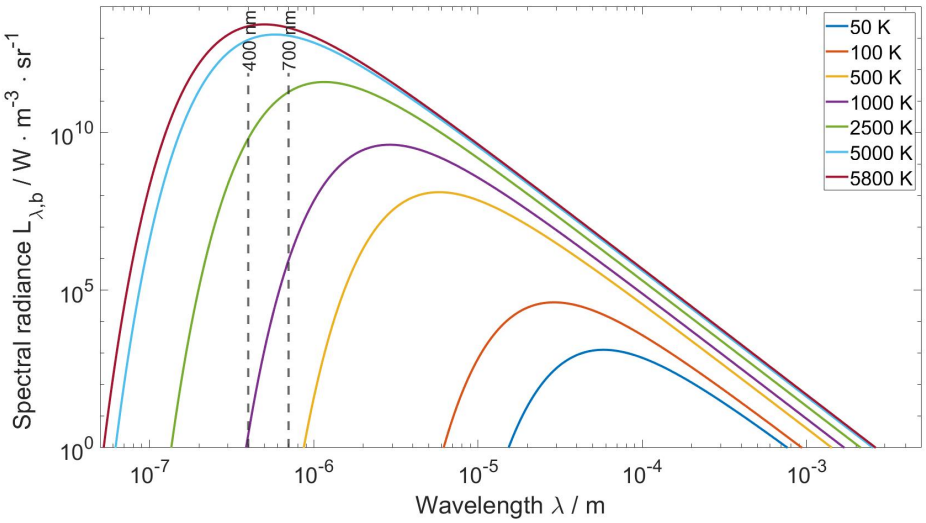

Figure 2.2: Spectral radiance of a black body for selected temperatures, calculated with Equation 2.10, visible range highlighted from 400 nm to 700 nm [11].

$$L_b = \int_0^\infty L_{\lambda,b}(\lambda)\mathrm{d}\lambda = \frac{\sigma}{\pi}T^4 \tag{2.13}$$

The constant σ is known as the Stephan-Boltzmann constant and can be defined with the two constants c_1 and c_2 by Equation 2.14. [9]

$$\sigma = \frac{c_1\pi^5}{15c_2^4} \tag{2.14}$$

Equation 2.8 is heavily simplified in case of a black body due to the directional independence. The spectral self-exitance for a black body can also be written as [9]

$$M_{\lambda,b} = \pi L_{\lambda,b} = \frac{c_1\pi}{\lambda^5}\cdot\left(e^{\frac{c_2}{\lambda\cdot T}}-1\right)^{-1}. \tag{2.15}$$

The total self-exitance is given by integrating the spectral self-exitance over all wavelengths or by using the first relation from Equation 2.15. [9]

$$M_b = \sigma \cdot T^4 \tag{2.16}$$

2.3 Radiation of a Real Body

To quantify the radiation of a real body the concept of emissivity is introduced. In some literature, a differentiation between emittance and emissivity is made. From the definition, emissivity describes the radiative property of an optically material with an uncontaminated surface. [9] The emittance on the other side is only defined for a particular object and is depending on properties of the object and especially of the surface. [12] Although the definitions are different, emissivity and emittance are commonly used interchangeably. [9, 12]

Emissivity is defined as the ratio of the radiance of a real radiant L_{em} to the radiance of a black body L_b for a certain wavelength, temperature and geometry. [13, 14]

$$\epsilon = \frac{L_{em}}{L_b} \tag{2.17}$$

The value of the emissivity is positive and equal or less than one ($0 \leq \epsilon \leq 1$) [8], because a black body always emits more radiation at a certain temperature T compared to any real surface. For most common applications the emissivity is between 0.1 and one. [15] Emissivity is dependent on the wavelength, the temperature and the geometry. An emissivity of one, describes a surface emitting the same radiance as a black body for a certain wavelength, temperature and geometry. Due to those dependences, many different definitions for specific radiation processes and measurement types exist. [13]

There are many different descriptors for emissivity but they can be grouped into geometric and wavelength descriptors. The order of these descriptors is not fixed. The main geometric descriptors are: [13]

- angular: describes a solid detection angle ω', with a directional angle of $\theta' \geqslant 15°$,
- normal: descriptor for a limiting case of angular, specifically for a solid detection angle ω' normal to the emitting surface, commonly used for angles of $\theta' < 15°$,
- hemispherical: descriptor for detection of flux Φ_{em} over a hemispherical surface, solid detection angle of $\omega' = 2\pi$.

Beside the 3 main descriptors concerning the geometry, other variations are commonly used. They usually describe a limiting case of a main descriptor.

The descriptor *directional* is used instead of *angular*, if the solid angle is negligibly small. In this limiting case, only the light, following a certain direction (θ', ϕ'), is detected. [13]

On the other hand *conical* is used as a descriptor for a limited but non-negligible solid angle $\omega' = \Omega < 2\pi$. For a complete description of this geometry, the direction of the cone, usually given by the angle pair (θ', ϕ'), and the size of the solid angle $\omega' = \Omega$, have to be specified. [13]

For the wavelength two main possibilities for the descriptor exist: [13]

- spectral: theoretically a description for one specific wavelength, but often used for a very small band of wavelengths,
- total: a descriptor that includes all wavelengths and is usually noted with a t.

If the spectral emissivity is known, the total emissivity can be calculated by integrating the spectral emissivity $\epsilon(\lambda)$ and the spectral self-exitance of a black body $M_{\lambda,b}(\lambda, T)$ over all wavelengths as shown in Equation 2.18. [13]

$$\epsilon(t) = \frac{\int_0^\infty \epsilon(\lambda) M_{\lambda,b}(\lambda, T) \mathrm{d}\lambda}{\int_0^\infty M_{\lambda,b}(\lambda, T) \mathrm{d}\lambda} \tag{2.18}$$

Similar to the geometric descriptors there is one additional descriptor used for the wavelength dependence. The descriptor *band-limited* [12] or *integrated* [13] is used, if not all wavelengths are considered. The integrals go from

one wavelength λ_1 to a second wavelength λ_2, spanning a continuous band of wavelengths.

2.3.1 Spectral Directional Emissivity

Spectral directional emissivity $\epsilon(\lambda;\theta',\phi';T)$ is defined as the ratio of the emitted radiance for a specific direction (θ',ϕ'), at a certain wavelength λ, by the surface $\mathrm{d}A$ and with a temperature T to the radiance of a black body with the same temperature for the same wavelength with an equal surface $\mathrm{d}A$. This relation is shown in Equation 2.19. [9]

$$\epsilon(\lambda;\theta',\phi';T) = \frac{L'_{\lambda,\mathrm{em}}(\lambda,\theta',\phi',T)}{L_{\lambda,\mathrm{b}}(\lambda,T)} \tag{2.19}$$

The notation used in Equation 2.19 was used in 1989, *DeWitt and Nutter* [9]. Analogous to 1989, *DeWitt and Nutter* [9] an abbreviated version of this notation will be used in the following chapters. For all further contemplations, the emissivity is temperature dependent. This fact makes it possible to imply the temperature for all notations. Additionally many optically homogeneous materials are isotropic in azimuth ϕ', therefore the emissivity can often be written as $\epsilon(\lambda;\theta')$. [9]

Spectral directional emissivity is the most basic form of emissivity and most other types of emissivity can be derived from Equation 2.19. [9]

Spectral normal emissivity[2], which was measured experimentally during this thesis, is a special case of the spectral directional emissivity. Specifically if the zenith angle is below 15° the descriptor *normal* is used. [13]

2.3.2 Total Directional Emissivity

Total directional emissivity is defined as the ratio of the spectral directional radiance integrated over all wavelengths to the spectral radiance of a black

[2]Outside of this introductory chapter, any time an emissivity is mentioned, it describes the normal spectral emissivity, if not stated otherwise.

body integrated over all wavelengths analogous to Equation 2.18. This relation is shown in Equation 2.20. [12, 16]

$$\epsilon(t;\theta',\phi';T) = \frac{\int_0^\infty L'_{\lambda,\mathrm{em}}(\lambda,\theta',\phi',T)\mathrm{d}\lambda}{\int_0^\infty L_{\lambda,\mathrm{b}}(\lambda,T)\mathrm{d}\lambda} \tag{2.20}$$

Equation 2.20 can be simplified using the Stephan-Boltzmann law, Equation 2.13.

$$\epsilon(t;\theta',\phi';T) = \frac{\pi \int_0^\infty L'_{\lambda,\mathrm{em}}(\lambda,\theta',\phi',T)\mathrm{d}\lambda}{\sigma T^4} \tag{2.21}$$

In the special case of a diffuse emitter, the directional emissivity is a constant for all directions. In many cases, a surface can be approximated as a diffuse emitter. It is to note though, that all real surfaces deviate at least slightly. The directional emissivity $\epsilon(\theta',\phi')$ for conductors can, in good approximation, be estimated as constant for zenith angles $\theta' \lesssim 40°$. At higher angles, the directional emissivity increases before decaying towards zero. A similar approximation can be made for non-conductors for angles $\theta' \lesssim 70°$. Compared to metals, the directional emissivity decreases instantly at higher angles. [16]

These observations mean that the directional emissivity and the spherical emissivity are very close value wise. The ratio $\epsilon(2\pi)/\epsilon(n)$ is mostly within the range of $0.95 \leqslant \epsilon(2\pi)/\epsilon(n) \leqslant 1.0$ for insulators and within the range of $1.0 \leqslant \epsilon(2\pi)/\epsilon(n) \leqslant 1.3$ for conductors. These ranges are valid for both, the total emissivity and the spectral emissivity for a certain wavelength. [16]

2.3.3 Spectral Hemispherical Emissivity

The spectral hemispherical emissivity is a weighted average for all directions within a hemispherical surface, normalized by the self-exitance of a black body. It is defined over the spectral self-exitance of the emitting surface and of a black body. [9]

$$\epsilon(\lambda;2\pi) = \frac{M_{\lambda,\mathrm{em}}(\lambda,T)}{M_{\lambda,\mathrm{b}}(\lambda,T)} \tag{2.22}$$

Using the definition of the total self-exitance (Equation 2.9), the spectral hemispherical emissivity (Equation 2.22) can also be calculated with Equation 2.23. [9]

$$\epsilon(\lambda;2\pi) = \frac{\int_0^{2\pi}\int_0^{\pi/2} L_{\lambda,\mathrm{em}}(\lambda,\theta',\phi',T)\cdot cos(\theta')\cdot sin(\theta')\mathrm{d}\theta'\mathrm{d}\phi'}{\int_0^{2\pi}\int_0^{\pi/2} L_{\lambda,\mathrm{b}}(\lambda,T)\cdot cos(\theta')\cdot sin(\theta')\mathrm{d}\theta'\mathrm{d}\phi'} \tag{2.23}$$

Considering the direction independence of the black body radiance and the definition of the emissivity (Equation 2.17), the spectral hemispherical emissivity can also be calculated with Equation 2.24. [9]

$$\epsilon(\lambda;2\pi) = \frac{L_{\lambda,\mathrm{b}}(\lambda,T)\int_0^{2\pi}\int_0^{\pi/2}\epsilon(\lambda;\theta',\phi')\cdot cos(\theta')\cdot sin(\theta')\mathrm{d}\theta'\mathrm{d}\phi'}{\pi L_{\lambda,\mathrm{b}}(\lambda,T)} \tag{2.24}$$

Under the assumption of a directional independence in the azimuth, a further simplification can be made. Then the spectral hemispherical emissivity is simplified to Equation 2.25. [9]

$$\epsilon(\lambda;2\pi) = 2\int_0^{\pi/2}\epsilon(\lambda;\theta')\cdot cos(\theta')\cdot sin(\theta')\mathrm{d}\theta' \tag{2.25}$$

2.3.4 Total Hemispherical Emissivity

The total hemispherical emissivity is defined as an average over all wavelengths for a hemispherical geometry. [9]

$$\epsilon(t;2\pi) = \frac{M_{\mathrm{em}}(T)}{M_{\mathrm{b}}(T)} \tag{2.26}$$

Analogous to the total directional emissivity (Equation 2.20) it can also be calculated from the spectral hemispherical emissivity $\epsilon(\lambda,2\pi)$ with an integral over all wavelengths. [9]

$$\epsilon(t;2\pi) = \frac{\int_0^{\infty}\epsilon(\lambda;2\pi)M_{\lambda,\mathrm{b}}(\lambda,T)\mathrm{d}\lambda}{M_{\mathrm{b}}(T)} = \frac{\int_0^{\infty}\epsilon(\lambda;2\pi)M_{\lambda,\mathrm{b}}(\lambda,T)\mathrm{d}\lambda}{\sigma\cdot T^4} \tag{2.27}$$

For the last result, Equation 2.16 was used to simplify the expression. [9]

3 Experimental Set-Up

In this chapter the experimental set-up and all measuring devices are explained. The experiments are performed with an ohmic pulse-heating apparatus (OPA) and different measurement systems can be used to detect several physical properties. The set-up is described in detail in many publications and theses, so in this chapter only a brief overview is presented. Additional information can be found e.g. in 1992, *Kaschnitz et al.* [17], 2001, *Seifter* [8], 2002, *Cagran et al.* [18], 2013, *Pottlacher et al.* [19] and 2017, *Leitner et al.* [20].

The main idea of the OPA is, to send a high electrical current pulse trough a wire-shaped sample and heat the sample because of its ohmic resistance. While heating, the sample melts and once it reaches the boiling point of the material, the wire explodes. This measurement technique enables measurements in the solid and the liquid phase.

To generate the current pulse (several 1000 A), a capacitor bank is charged with 35 mA to the target voltage, which is material dependent. This voltage is typically in the range of 5 - 6 kV but in theory the capacitor bank could be charged up to 10 kV [8].

Because of the short periods of the experiment (µs), the wire stays in shape after melting and explodes once the gas phase is reached. Chemical reactions on the surface of the sample are avoided for the most part because of the short time scales of the experiment and the fact that all experiments are performed in a nitrogen atmosphere. [21]

The switching-on and switching-off processes are managed with two ignitron tubes with two krytrons as switching elements. It is necessary to use ignitrons because of the combination of short time scales, high voltages and high currents. Switching times of 0.2 µs are reached but require a supply

voltage of 3 kV for the ignitrons. Inside the ignitrons, a mercury bath is used as a cathode. For operation, the mercury bath is heated with two infrared lamps beforehand. A more detailed description of the ignitrons and krytrons, how they work and how they are used in this apparatus, can be found in 1992, *Kaschnitz* [22].

Once the capacitor bank is at the required voltage, the experiment is started manually. The data acquisition starts immediately. The first ignitron is triggered after a predefined time, usually around 190 µs, and sends the current through the wire, therefore starting the experiment. The second igniton is triggered after a defined experiment time, usually around 40 µs, ending the experiment by grounding the capacitors through a resistor with 0.5 Ω.

During this experiment, several physical properties can be measured with different detection systems. The current through the wire is measured with a measuring coil from Pearson Electronics, Inc. and the voltage over the length of the wire could be measured by mounting two cutting edges on the sample. A pyrometer is aimed at the wire to measure the radiance temperature of the wire to determine temperature dependencies of other physical properties. The third measurement device used, is a microsecond Division of Amplitude Photopolarimeter (µs - DOAP). It enables the measurement of the index of refraction, the extinction coefficient and consequently also the normal spectral emissivity by measuring the change of polarization at the reflection.

In Figure 3.1, a photograph of the main part of the measurement system is shown. The laser light moves from the left hand side through the PSG and towards the sample chamber. The laser light enters and exits the sample chamber through two BK-7 windows, which do not change the polarization state. The wire is fixed in the middle of the sample chamber. The laser light is reflected at the wire and then the PSD detects the reflection at an angle of 140°. Additionally a pyrometer is aimed towards the wire. The pyrometer can be seen at the bottom of the picture. On the back side of the sample chamber two tubes are connected to rinse the sample chamber with nitrogen to generate a controlled atmosphere.

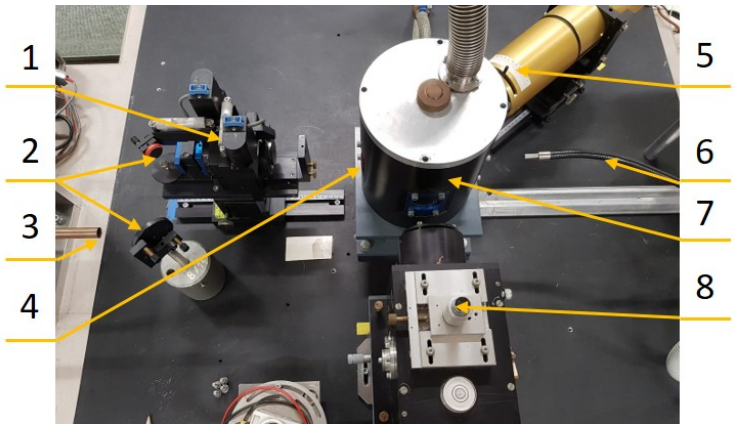

Figure 3.1: Photograph of the sample chamber and the different measurement systems used, 1: polarization state generator (PSG), 2: mirrors to guide the laser, 3: tip of the box, containing the laser, 4: Bk-7 window for laser, 5: polarization state detector (PSD) , 6: light to adjust pyrometer, 7: sample chamber, 8: 649.7 nm pyrometer.

3.1 General

All measurement devices send their output signal to a computer for further processing. Two different computers are being used for the two measurement devices. One computer is in charge of the DOAP evaluation, the other computer receives the pyrometer, the current, and potentially the voltage signals. These computers are inside a measurement cabin, positioned outside of the main laboratory. With copper seals on the door, the cabin is sealed off from electromagnetic radiation, which is created during the experiment.

Not only the measurement cabin is sealed off from electromagnetic radiation but also all wires, which carry a signal from a measurement device to the measurement cabin, are in a copper encasing to protect the information from electromagnetic radiation.

The generator, which charges the capacitor bank, is situated outside of the main laboratory. The control panels are also outside to start and control the experiment from safe distance. This is necessary because high voltages and currents are used during the experiments.

A multimeter measures the voltage on the capacitor bank. The final voltage reaches up to several kV, so a voltage transformer is installed that divides the voltage by a factor of 276 and the scaled down voltage can be measured with a multimeter.

3.2 Sample Chamber

A wire-shaped sample is placed vertically in a sample chamber. The sample chamber itself has two glass windows and two BK-7 windows. One glass window is used for the pyrometer to determine the temperature of the wire and the BK-7 windows are used for the laser because they do not change the polarization. Both BK-7 windows differ in size but have the same thickness of 3 mm. All windows are sealing off the sample chamber from gas with a circular sealing.

The sample chamber itself consists of two different parts. After each experiment, both parts are removed for cleaning. The outer part has the windows and the connections for the nitrogen. The inner part is used to fix the wire and is then placed inside the outer part. Four screws on top hold the chamber in place. A circular sealing on top seals off the sample chamber once it is fully constructed. The complete sample chamber can be seen in Figure 3.1. The inner part of the sample chamber with an installed wire can be seen in Figure 3.2.

To get acceptable results, the wire needs to be installed with some tension because otherwise, the wire could move or deform once it reaches the liquid phase. The tension is introduced manually during the installation of the wire by pushing the top and bottom clamp apart and fixing them while the pressure is applied.

On the bottom of the sample chamber, electric connections establish a connection to the current measurement coil. Two gas valves are positioned on the side of the sample chamber to flush it. During the experiments a nitrogen atmosphere was used with a pressure of 1.3 bar.

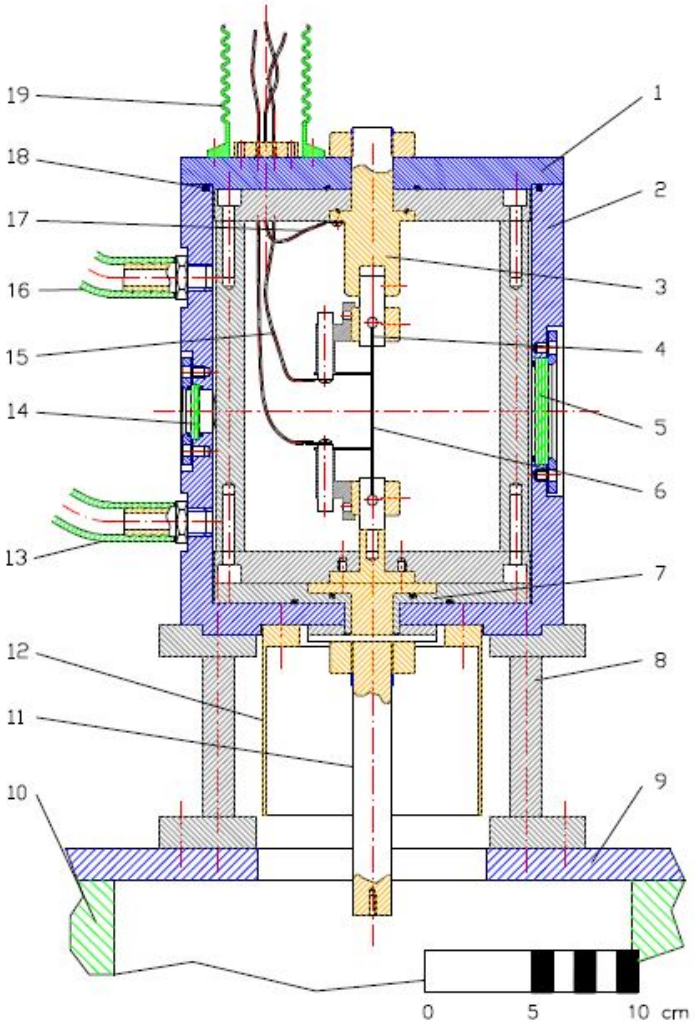

Figure 3.2: Schematic of the sample chamber, 1: housing, 2: wire clamping, 3: clamping device, 4: aluminium cover, 5: wire (sample), 6: glass window for pyrometer, 7: BK7-window for laser, 8: insulation for current feed-through, 9: bracket, 10: aluminium plate, 11: concrete table, 12: power option guide, 13: current lead, 14: gas hose, 15: voltage measurement wire, 16: ground potential, 17: o-ring, 18: measuring disc, 19: flexible hose for electromagnetic shielding. Figure adapted from 2001, *Seifter* [8].

3.3 Pyrometer

The International Temperature Scale of 1990 (ITS-90) [6] defines temperature above the melting point of silver (1234.93 K) by spectral pyrometry. The pyrometer is essential in this set-up because it allows a measurement of the radiance temperature of the wire in the solid and liquid phase.

Every object, which is not at a temperature of absolute zero (0 K), is constantly emitting thermal radiation. A pyrometer is used for detecting this radiation. The radiance temperature can then be calculated from the voltage signal.

During the experiments of this thesis, an especially designed pyrometer for very fast time responses, for radiation with a wavelength of 649.7 nm with a full width at half maximum of 37.2 nm, is used. This pyrometer allows the measurement of radiance temperatures from about 1650 K to about 3300 K.

The pyrometer produces a voltage signal U, which is temperature dependent. Despite the temperature dependence, it is not easy to calculate the temperature directly because the signal is, amongst other dependencies, influenced by a geometrical parameter. The output signal is given by: [8]

$$U(T) = V \cdot G \int_0^\infty \sigma(\lambda) \cdot \tau(\lambda) \cdot \epsilon(\lambda, n) \cdot L_\lambda(\lambda, T) \mathrm{d}\lambda. \tag{3.1}$$

V ... sensitivity of the electric circuit / V/W
G ... geometry factor
σ ... spectral sensitivity of the detector
τ ... permeability of the optical system

Many of these factors are not known and cannot be measured easily. Therefore, a manual calibration is made during the evaluation. A point, at which the radiance temperature is known, is taken as a reference and the signal is adjusted. Mathematically this yields a temperature dependent calibration constant K with which the radiance temperature for the entire signal can be calculated with Equation 3.2. [8]

$$T_{\mathrm{rad}} = \frac{c_2}{\lambda \cdot \ln\left(\frac{K}{U} + 1\right)} \tag{3.2}$$

For most materials, the radiance temperature at the melting point can be found in the literature. During evaluation, the calibration constant is calculated and the temperature-time dependence is adjusted accordingly.

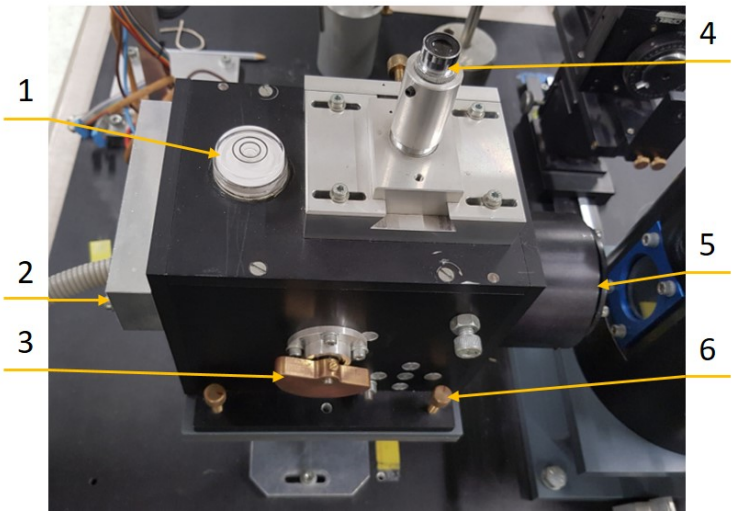

Figure 3.3: Photograph of the pyrometer used, 649.7 nm, 1: spirit level, 2: clarity adjustment screw, 3: rotatable mirror, 4: measurement microscope, 5: optical lens system, 6: levelling adjustment screw, a schematic of a pyrometer can be found in 2001, *Seifter* [8] or 2004, *Cagran* [21].

From the radiance temperature, it is possible to calculate the real temperature of the radiating surface with the concept of the emissivity. The radiance temperature T_{rad} is the temperature a black body has, if it emits the same radiance as a real body with the temperature T. Considering this definition of the radiance temperature, the spectral normal emissivity can be written as Equation 3.3. [8]

$$\epsilon(\lambda, n, T) = \frac{L_{\lambda,\mathrm{b}}(\lambda, T_{\mathrm{rad}})}{L_{\lambda,\mathrm{b}}(\lambda, T)} \tag{3.3}$$

This observation also indicates that the radiance temperature is always lower than the real temperature because at the same temperature, a black body always has a higher radiance.

In practice, neutral-density filters are used to lower the total intensity of the radiation in front of the pyrometer. At a certain intensity, the pyrometer reaches saturation and no measurements at higher intensities are possible. The neutral-density filter lowers the intensity equally over all wavelengths and this allows the measurement of higher temperatures. On the downside, the pyrometer starts working at higher temperatures and measurement points are lost in the solid phase. Primarily, the choice of neutral-density filter is material dependent because of the different melting temperatures and the different normal spectral emissivities. If for example only the liquid phase is investigated, the measurement points in the solid phase are not needed and a high neutral-density filter can be used.

3.4 Photopolarimeter

For this thesis, a photopolarimeter was used to determine the spectral directional emissivity. Common polarimeters rely on mechanically moving parts. This movement hinders the resolution due to the limited mechanical movement per time. The polarimeter used, was described by 1982, *Azzam* [7] and added to this apparatus in 2001, *Seifter et al.* [23]. It works without any moving or rotating parts during the measurement and therefore provides a high resolution.

The polarimeter consists of three main parts, which will be described in this chapter. A laser is used as a light source, a polarization state generator (PSG) generates a predefined linear polarized state and after the reflection on the sample, a polarization state detector (PSD) detects the reflected light.

Coherent light is produced by the laser, which is then directed through the PSG to change the polarisation of the laser to a predefined direction. Then the laser hits the wire and is reflected. During this reflection process, the polarization changes. The PSD detects the reflected light beam and the change in polarization can be calculated by comparison of the original and the detected polarization. From the change in polarization the two ellipsometry parameters ψ and Δ can be calculated. They define the index of refraction n_2 and the extinction coefficient k_2 of the reflecting sample.

Finally the normal spectral emissivity $\epsilon(\lambda, n, T)$ for the wavelength of the laser can be calculated.

3.4.1 Polarized Light

For the polarimeter measurements, polarized light is required. Polarized light can be created from natural light by interactions with matter. These interactions can favour a certain direction of polarization and therefore create polarized light. Polarization can be described by the polarization ellipse, which is defined over the front view of the tip of the electric field. The polarization ellipse can be described by four Stokes parameters S_0 - S_3. [24] It is also possible to describe the polarization ellipse with the main axis a, the minor axis b and the azimuth angle ψ of the ellipse. [8]

For monochromatic light, S_0 is not independent and can be calculated from the three other Stokes parameters with Equation 3.4.

$$S_0^2 = S_1^2 + S_2^2 + S_3^2 \tag{3.4}$$

All Stokes parameters can be calculated from intensities of the light beam. S_0 is a measure of the total intensity of the light beam. S_1 is given by the difference of intensities between the horizontal and vertical linear polarized light. S_2 can be calculated from the difference between the intensities of the +45° polarized and -45° polarized components of the light. S_3 describes the difference between the right (RCP) and the left (LCP) circular polarized light. [8, 24]

$$\begin{aligned} S_0 &= I_{\text{tot}} = I(0^\circ) + I(90^\circ) \\ S_1 &= I(0^\circ) - I(90^\circ) \\ S_2 &= I(+45^\circ) - I(-45^\circ) \\ S_3 &= I(RCP) - I(LCP) \end{aligned} \tag{3.5}$$

The degree of polarization P describes the deviation from Equation 3.4. From an experimental standpoint, the positioning of the different components is

aimed at a degree of polarization of one. [8]

$$P = \frac{S_1^2 + S_2^2 + S_3^2}{S_0^2} \tag{3.6}$$

Any single interaction of light with an optical element can be described by a Mueller matrix. If there are several optical elements, the total interaction can be calculated by multiplying the corresponding matrices and then applying this matrix to a Stokes vector, which describes the polarized light. The Mueller matrix, describing reflection on a surface, is shown in Equation 3.7 with the ellipsometry angles ψ and Δ and the norm of the complex reflection coefficient for the parallel wave part ρ_p and the normal wave part ρ_n. [8, 25]

$$M_\mathrm{refl} = \frac{\rho_\mathrm{p}^2 + \rho_\mathrm{n}^2}{2} \begin{pmatrix} 1 & -\cos(2\psi) & 0 & 0 \\ -\cos(2\psi) & 1 & 0 & 0 \\ 0 & 0 & \sin(2\psi)\cos(\Delta) & \sin(2\psi)\sin(\Delta) \\ 0 & 0 & -\sin(2\psi)\sin(\Delta) & \sin(2\psi)\cos(\Delta) \end{pmatrix} \tag{3.7}$$

3.4.2 Mathematical Determination of the Emissivity

Starting inside the detector, the light is split into four different beams and their intensities I_0 - I_3 are detected separately with photo detectors. The vector of intensities describes the Stokes vector $\vec{S}$ together with the device matrix $\overleftrightarrow{A}$. [8]

$$\vec{S} = \overleftrightarrow{A}^{-1}\vec{I} \tag{3.8}$$

To measure the device matrix 18 linear independent polarizations and 36 circular polarized states for the laser are generated and the intensities are measured. This generates an overdetermined system of equations, which allows the calculation of the device matrix from calibration.

The ellipsometry parameters are calculated with the help of the Mueller matrix $\overleftrightarrow{M}_\mathrm{refl}$, which describes the reflection on a surface. Therefore, the

Stokes vector of the reflected light $\vec{S'}$ can be calculated with Equation 3.9. [8]

$$\vec{S'} = \overleftrightarrow{M_{\text{refl}}}\vec{S} \tag{3.9}$$

With the Mueller matrix for reflection, shown in Equation 3.7, both ellipsometry angles can be calculated from the entries of the Stokes vector S_{i} of the reflected beam with Equation 3.10 and Equation 3.11. [8]

$$\tan(\Delta) = -\frac{S'_3}{S'_2} \tag{3.10}$$

$$\tan(2\psi) = -\frac{\sqrt{S'^2_2 + S'^2_3}}{S'_1} \tag{3.11}$$

To simplify the calculation of the normal spectral emissivity and the uncertainty analysis, the two axis of the polarization ellipse a and b can be used as intermediate results. The angle θ describes the angle, at which the reflected light is detected. [26]

$$a = n_1^2 \cdot \sin(\theta)^2 \cdot \left[1 + \tan(\theta)^2 \cdot \frac{\cos(2\psi)^2 - \sin(2\psi)^2 \cdot \sin(\Delta)^2}{(1 + \cos(\Delta) \cdot \sin(2\psi))^2}\right] \tag{3.12}$$

$$b = n_1^2 \cdot \sin(\theta)^2 \cdot \tan(\theta)^2 \frac{\sin(2\psi) \cdot \cos(2\psi) \cdot \sin(\Delta)}{(1 + \cos(\Delta) \cdot \sin(2\psi))^2} \tag{3.13}$$

With the help of the intermediate results from Equation 3.12 and Equation 3.13 it is now possible to calculate the index of refraction n_2 and the extinction coefficient k_2 of the reflecting sample with Equation 3.14 and Equation 3.15. [26]

$$n_2 = \sqrt{(1/2 \cdot (a + \sqrt{a^2 + b^2})} \tag{3.14}$$

$$k_2 = \sqrt{(1/2 \cdot (-a + \sqrt{a^2 + b^2})} \tag{3.15}$$

Using this complex index of refraction $\eta_2 = n_2 - \mathrm{i} \cdot k_2$, the normal spectral emissivity can be calculated with Equation 3.16. [5]

$$\epsilon(\lambda, n, T) = 1 - \frac{1 - 2n_2 + n_2^2 + k_2^2}{1 + 2n_2 + n_2^2 + k_2^2} \tag{3.16}$$

3.4.3 Laser

First of all a laser is producing the coherent light needed for the measurement. The laser used, produces light with a wavelength of 684.5 nm. It is in a metallic box to protect the laser and the control electronics from electromagnetic radiation. The box is fixed on the table and two mirrors are used to guide the laser beam through the PSG and towards the wire. The positioning of the mirrors has to be chosen carefully to generate a completely horizontal laser light through all optical components. Within the box, a spirit level is used to ensure the horizontal orientation of the laser.

In this case, the laser light is produced by a laser diode. Therefore, the laser is linear polarized. This can cause a problem if the PSG is set to a certain direction of polarization because the resulting intensity could be too small. To account for this problem, the laser light is sent through a $\lambda/4$ plane to change the type of polarization from linear to circular. [8]

3.4.4 Polarization State Generator

For the measurement but also for the calibration, predefined polarization states are needed as a reference. The linear polarization is produced by the PSG, which can be rotated with a stepping motor to change the direction of the linear polarization. For the calibration, circular polarized states are also required and therefore an additional retarder can be mounted in front of the PSG. The retarder can be rotated independently with a second stepping motor to vary the circular polarization. For normalization, a reference detector is needed to measure the total intensity before the reflection. This reference detector is attached after the main PSG instead of the lens used during the measurement (see Figure 3.5).

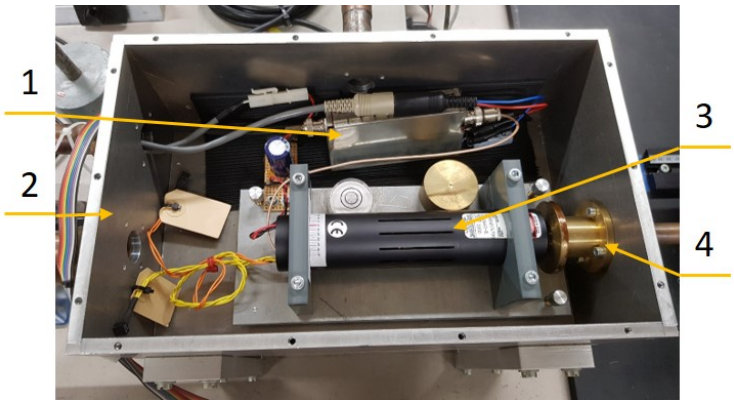

Figure 3.4: Photograph of the 684.5 nm laser inside an opened metal box, 1: control electronic, 2: metal box for radiation protection, 3: laser cavity, 4: output out laser into measurement system.

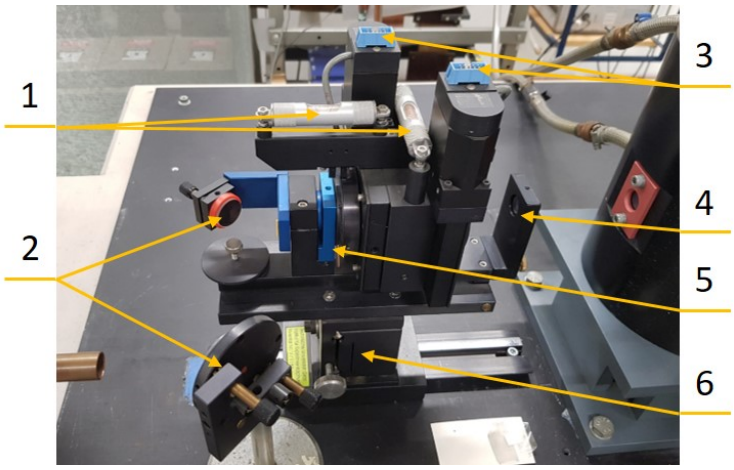

Figure 3.5: Photograph of the polarization state generator (PSG), 1: spirit level, 2: adjustable mirrors, 3: cable connections for stepping motors, 4: focusing lens, switched with a reference detector during calibration, 5: $\lambda/4$ glass, 6: adjustable base, a schematic of the PSG used can be found in 2001, *Seifter* [8] or 2004, *Cagran* [21].

The PSG is mounted on an adjustable base. Both tilting directions in the horizontal plane can be adjusted. Two spirit levels on top of the PSG show a potential tilting, which has to be accounted for. The distance of the PSG to the wire can be adjusted by sliding the base with the PSG on a rail. The PSG can also be shifted normal to the direction of the light, to adjust the

outgoing laser.

3.4.5 Polarization State Detector

The detection of the polarized light is done with a PSD. A cover in front of the detector is used to block light, which is not reflected at the correct detection angle. The cover can be opened and closed continuously and the size of the aperture determines the spread of light, which can enter the detector. Within the detector, the laser beam is first split into two parts [25] and then each part is split again into their perpendicular polarized components with a Glan–Thompson prism [8]. All four parts of the laser are focused on individual photo-detectors. In addition, the transfer of the data happens separately with four different optical fibres. The signal is converted and read in the computer separately to determine the Stokes vector.

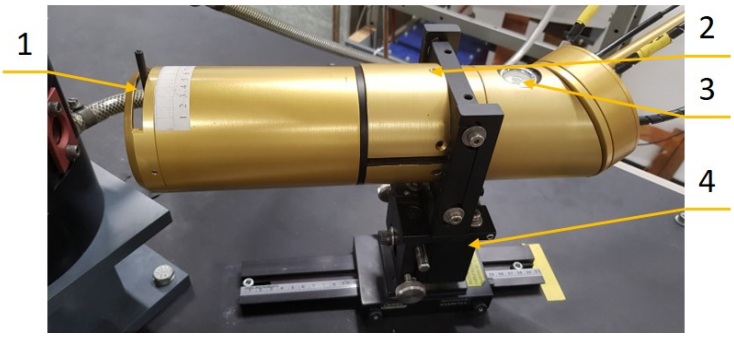

Figure 3.6: Photograph of the polarization state detector (PSD), 1: front cover, 2: cover, if removed allows access to check for focus, 3: spirit level, 4: adjustable base, a schematic of the PSD used can be found in 2001, *Seifter* [8] or 2004, *Cagran* [21].

The detector itself is mounted on an adjustable base. First, the distance of the detector to the wire can be changed. Secondly, the PSD can be tilted in both, horizontal and vertical, directions. The angle in the horizontal plane is fixed during calibration and the detector should always stay parallel to the ground, so the vertical angle has to be adjusted if needed. The PSD can also be shifted normal to the direction of the light, to adjust the detector to the incoming laser. In addition, the height of the detector can be varied depending on the incoming laser. Because some of those adjustments are

depending on the position of the wire, they have to be adjusted before every experiment. On the other hand, some parameters, especially the angle of the PSD, have to be constant over all experiments, are set during calibration, and are controlled occasionally to ensure comparability.

4 Experimental Preparation

In this chapter very important tasks are described to ensure comparable measurements and a correct result. Most of these tasks must be performed prior to any experiment.

Before experimenting with the μs-DOAP, the device matrix has to be found in order to measure the normal spectral emissivity. The device matrix is determined experimentally by performing a calibration measurement. Once the device matrix is known, the apparatus is switched into measurement position. To set the correct angle of the PSD with respect to the PSG, test measurements with a BK-7 prism are performed and the result is manually compared to the theoretical result. Between each test measurement, optical components are repositioned slightly until the measurements match the theoretical values. Afterwards the BK-7 prism is replaced with the sample chamber and a wire-shaped sample can be installed.

Prior to any experiment, the wire-shaped sample has to be prepared with abrasive paper and acetone to allow measurements in the solid phase. Then the sample has to be installed and only one experiment can be performed with every sample because the sample explodes during the experiment.

Within this chapter also a step by step explanation of a typical experimental sequence is provided. It describes every single step, necessary for an experiment with the μs-DOAP and goes into detail of different waiting times and typical time frames.

In the last part of this chapter some additional methods are explained to achieve comparable results. Additionally, useful tips are provided for certain steps during the preparation.

4.1 Calibration of the μs-DOAP

A calibration is needed in this experimental set-up to account for all unknown optical components in the laser path. This is necessary because the optical components cannot be described with ideal Mueller matrices because of insufficient information. All unknown parameters are summarized in one 4x4 device matrix $\overleftrightarrow{A}$. During calibration, the first three columns of the device matrix are calculated from 36 linear polarized states. The fourth column is calculated from 36 circular polarized states, 18 left and 18 right polarized. Altogether, an overdetermined system of equations is solved with a Least-Square routine to determine the device matrix.

This device matrix is needed for the evaluation of the measurements according to Equation 3.8. With this equation, the Stokes vector can be determined through the measured intensities. During this calculation, it is necessary to invert the device matrix, so the device matrix has to be a regular matrix.

The process of calibration was mostly performed according to 2001, *Seifter* [8]. In this chapter only a brief overview is provided and a more detailed discussion can be found in 2001, *Seifter* [8].

For the calibration, the PSG and the PSG have to be oriented opposite to each other, so at an angle of 180°. This position is shown in Figure 4.1. With two mirrors, the laser is directed through the PSG, straight towards the centre of the PSD. The laser itself has to be completely horizontal and the laser beam has to go centrally through all optical components. This is checked with plastic covers with a small hole in the centre, to let the laser through. With this very simple but effective method, a slight deviation can be registered anywhere in the optical path.

In the front of the PSD a reference detector is mounted to measure the total intensity of the laser. In the front of the PSG a lens with a focal length of f= 145 mm [8] is used. The distance of the PSD to the position of the sample is adjusted by focusing the laser beam at the position of a future sample. Afterwards, the PSD is adjusted to the laser beam and its direction. This is done by moving the PSD normal to the laser to centre the laser beam on the detector. Finally a $\lambda/4$ plane is inserted in front of the PSG. This plane converts the linear polarized light of the laser into circular polarized

light, which is then sent through the PSD. This step is necessary to achieve a higher intensity of the linear polarized light.

Before starting the calibration itself, the controls for two stepper motors are attached to vary the direction of the linear polarized light. During calibration, 36 linear polarized states are generated without the $\lambda/4$ plane and then 18 left and 18 right circular polarized states are generated with the $\lambda/4$ plane to determine the device matrix with a Least-Square routine.

On the measurement computer, an offset-calibration is performed, to subtract the natural light from the signal because the reference detector cannot differentiate different wavelengths. Therefore, the room is dimmed and the lights are switched off during the experiment. To avoid saturation, the signal of the reference detector has to be below 2 V but above 0.2 V for an acceptable result.

The mathematical description for the calculation of the device matrix can be found in Chapter 6.3.2 in 2001, *Seifter* [8].

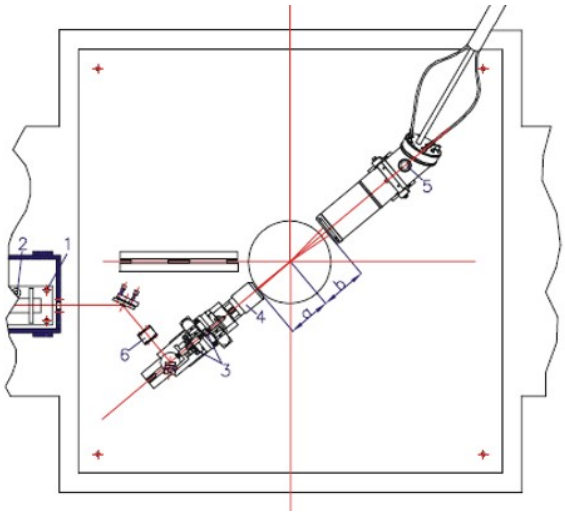

Figure 4.1: Schematic of the optical components during the calibration, 1: screws to adjust laser, 2: spirit level of laser, 3: spirit levels of PSG, 4: reference detector, 5: spirit level of PSD, 6: retarder, a: working distance of PSG and reference detector, b: working distance of PSD (145 mm). Figure adapted from 2001, *Seifter* [8].

To evaluate the device matrix, a verification is performed. During this verification, selected polarization states are generated and the measurements

are compared to the theoretically calculated Stokes parameter $S_1 - S_3$. Then the deviation S_i *Error* is calculated. During the calibration, this deviation is minimized by making small adjustments to the optical components. According to 2001, *Seifter* [8] the limit of S_i *Error* is 0.015 and a calibration is considered good, if the deviation is lower than 0.005. Another key value of the verification is the root mean square error (*RMS Error*). It should be below 0.020 and a good calibration is achieved if the root mean square error is below 0.009.

A further evaluation of the calibration can be performed with additional outputs from the calibration process. Beside the S_i *Error* and the *RMS Error*, the standard deviation of the circular polarized states should be below 1.5 and a calibration is considered good, if the value is below 1.135. Another check can be made with the *consistency*, a deviation of the first column between the calculation with linear polarized and circular polarized light, in percent. The limit of the *consistency* is 2 and for a good calibration the value should be below 0.840.

Although it is possible to get below the individual values of a good calibration, in practice it is highly unlikely to get a good calibration according to all values. Therefore, typically all values are minimized as good as possible and a compromise between the different values has to be found.

4.2 Experimental Position of the PSD

During the measurements, an angle of 140° between the PSG and the PSD is required. To achieve a high accuracy of this angle, test measurements with a BK-7 prism are performed and the results are compared to theoretically calculated values.

Analogous to the previous chapter the positioning was mostly performed according to 2001, *Seifter* [8]. Again, only a brief overview is provided and a more detailed discussion can be found in 2001, *Seifter* [8].

First of all, the linear polariser is rotated to a position of +45° from the control panel at the computer in the measuring booth. Afterwards both stepping motors are disconnected and the reference detector is removed. In

front of the PSG, a converging lens, with a focal length of 170 mm, is fixed. During the calibration, the PSG was positioned opposite to the PSD. For the measurements, the PSG is positioned on a second rail, mounted on the table, at an angle of about 140° with respect to the PSD. Also the second rail can be seen in Figure 4.1. The position of the PSG is important because the laser has to be focused on the future position of the wire.

At this point, it is important to adjust all optical components to be completely horizontal with the help of spirit levels. Also the position and the direction of the laser is important, because the laser beam needs to go centrally through all optical components.

After the position of all optical components is adjusted, a BK-7 prism is used instead of the wire-shaped sample to adjust the angle to 140°. First of all, the prism is turned in a way, that the laser is reflected back into the PSG again (lower laser beam in Figure 4.2). Therefore, the laser beam has to hit all optical components in the centre and the laser has to be completely horizontal. Afterwards, the PSG is shifted slightly to the left, until the laser hits approximately the centre of the angled surface (upper laser beam in Figure 4.2).

Now the adjustments of the PSD start. To achieve the correct angle, a live measurement is started on the computer and the values are constantly compared to theoretical values. By moving, tilting and adjusting the PSD, the theoretical values can be reached with an iterative process. Extra time should be taken for these steps, to achieve a precise angle because the measurement of the spectral normal emissivity strongly depends on the angle.

Because the PSD is adjusted to the position of the wire before every experiment, only the angle has to be adjusted precisely. During the positioning it became apparent, that especially the spectral normal emissivity ϵ and the index of refraction n are highly dependent on the angle. On the other hand, the degree of polarization $degP$ is more dependent on the vertical and horizontal positioning of the PSD and the precise entry of the laser beam into the PSD.

Originally, the mirrors were flipped during the calibration process to direct the laser towards the sample chamber. However, with a slight rearrangement

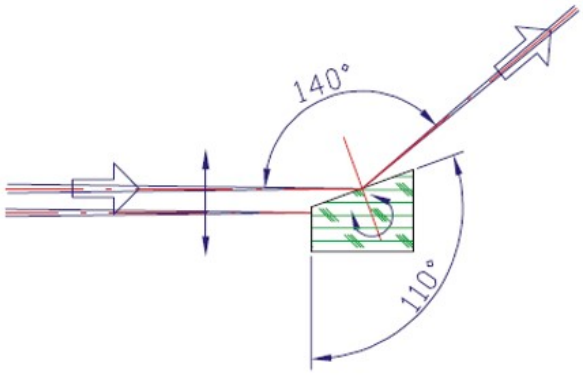

Figure 4.2: Schematic of the BK-7 prism and the laser light in measurement position. The upper laser beam hits approximately the center of the angled plane and the reflection hits the PSD. The lower laser beam is reflected back to the PSG. Figure adapted from 2001, *Seifter* [8].

it is possible to keep the mirrors in the measurement position during calibration as well. Also the laser was rotated for about 90° to achieve a higher intensity during calibration. After calibrating without turning the laser, the intensity turned out perfectly fine and no measurable difference could be found. Therefore, the laser was kept in measurement position during the calibration, to ensure equal conditions for the calibration and the measurement. The $\lambda/4$ plane, in front of the PSG, was kept in its position during the entire calibration process and also during the measurements.

4.3 Sample

In this chapter, different aspects surrounding the sample are explained in detail. This includes the sample preparation before every experiment and afterwards the sample installation in the sample chamber. All measurement devices are aligned with the installed wire before every single experiment because the wire cannot be installed at exactly the same position every time.

4.3.1 Sample Preparation

Before any experiment can be performed, the sample has to be prepared. First of all, the wire is cut to the correct length, which is about 5 cm. Then the wire is straightened for the first time and fixed in the bottom clamp of the sample chamber. Afterwards, the wire is straightened for the second time. At this point the wire should be as straight as possible without any structural damage or kinks. In the last step, abrasive paper (grade 1200) is used to roughen the surface before cleaning the wire with acetone.

During this procedure it is important to remain consistent between the different experiments. Therefore, abrasive paper was used a certain amount of times (8, 16, 24), rotating the wire 45° after every application. The amount of applications was determined by the softness of the material but consistent across all experiments for one material. Also the application of acetone was kept consistent between the different experiments for a certain material to ensure comparability.

After the wire is cleaned, the wire and the clamps are fixed inside the inner part of the sample chamber, which is then built-into the experimental apparatus itself.

4.3.2 Sample Installation

Before every measurement, the optical devices are adjusted to the position of the built-in wire. Because the outer part of the sample chamber is taken out for cleaning and the windows are replaced after every single experiment, the orientation of the sample holder has to be adjusted during the installation. This is critical because the laser beam and the pyrometer need to be perfectly perpendicular to the associated windows. The easiest way to ensure the proper installation is to let the laser beam reflect back onto itself. This can for example be checked with a piece of cardboard with a small hole in it.

Once the sample is cleaned and installed in the inner part of the sample chamber, both parts of the sample chamber are merged, sealed off and fixed with four screws on top. The next step is to align the polarization state generator (PSG) to the wire in a way, that the intensity of the reflection,

reaching the front cover of the polarization state detectors (PSD), is as high as possible. Then the PSD is aligned to the reflection. The goal is to register the highest possible intensity at the detector and to get a degree of polarisation of one. The intensity at every channel of the detector has to be above 0.2 Volt and below 2 Volt. Otherwise the detector is outside of its limits and the measurement process might fail. The cover of the PSD was left half open during all measurements.

4.4 Experimental Sequence

This chapter describes a typical experimental sequence from the start, to the data evaluation. During the experiments, experimental logs were used to keep track of the different settings and surface preparations for every single experiment.

Usually the preparations for the experiment start in the morning. If the polarimeter is used, the laser needs to run for about four to five hours before any experiment can be conducted. Therefore, theses steps have to be performed hours before any measurement:

- computer: in the morning, the two measurement computers are switched on, their time and date is set and the control panel of the DOAP is started. Afterwards, a manual background subtraction is performed,
- laser: the power supply of the laser is switched on and the different covers of all optical components can be removed,
- adjustments: all optical components are checked for potential displacements with their respective spirit levels. Then the path of the laser is checked to ensure, that the laser hits the optical components centrally.

At this point, the laser needs to run for at least four to five hours in order to reach a constant intensity over time. During this time, the wire-shaped sample can be straightened for a first time and the equipment can be checked. After about four and a half hours, the final preparation for the experiments can start:

- nitrogen: the valves on the high-pressure gas tank, filled with nitrogen, are opened and the pressure is checked,

- infrared lamps: in order to use the ignitrons, infrared lamps are used to heat the mercury bath. The infrared lamps need to run for about half an hour before the first experiment,
- time management: the different timings for the experiments are set, depending on the material,
- neutral-density filter: depending on the material, a neutral-density filter is chosen and put on an optical mount.

With the experimental apparatus prepared, the experiments can start. The following points have to be performed for every experiment separately:

- sample preparation: the wire shaped sample is treated with abrasive paper (grade 1200) and acetone to roughen up the surface,
- sample installation: the sample is fixed inside the inner part of the sample chamber with tension. Then the inner part of the sample chamber is installed inside the outer part,
- nitrogen atmosphere: the sample chamber is flushed with nitrogen for about a minute. Afterwards the sample chamber is kept at a constant pressure of 1.3 bar,
- pyrometer: the pyrometer is adjusted to the position of the wire. For illumination, an additional light source is used, the *1.0* in the measurement microscope of the pyrometer should be right in the centre of the wire. Afterwards, a neutral-density filter can be installed in front of the pyrometer if required,
- PSG: the PSG is adjusted in a way, that a maximum of the reflection is visible on the cover of the detector,
- PSD: the PSD is adjusted in a way, that the light passes through the aperture centrally and directly into the detection mechanism. This is checked with the DOAP software on the measurement computer inside the measurement chamber,
- software: the computers are prepared by triggering them to the manual start of the experiment,
- measurement chamber: the measurement chamber is sealed off against electromagnetic radiations,
- ignitrons: the ignitrons are switched on,
- infrared lamps: the infrared lamps are switched off with a timer for the duration of the experiment,

- grounding: the grounding devices are removed allowing a voltage to build up on the capacitor bank.

At this point, the main laboratory is cleared and the next steps are performed from outside of the laboratory:

- generator: the generator is switched on and the material dependent target voltage is generated on the capacitor bank. A reduced voltage, by a factor of 276, is monitored over a multimeter,
- start of experiment: once the target voltage is reached, the generator and the multimeter are switched off and the experiment is triggered manually.

From outside of the laboratory a short flash of light and a soft bang are witnessed. Afterwards the experiment is done. At this stage, it is important to check the remaining voltage and getting rid of any left-over energy:

- voltage check: the multimeter is switched back on and the remaining voltage is measured. Once the voltage is below 0.3 V,
- grounding: first a string is pulled to short the capacitor bank and then a hook is used to ground the whole set-up, another soft bang is heard when the capacitor bank is grounded spontaneously. Afterwards no voltage should remain on the capacitor bank.

Once no voltage is remaining on the capacitor bank, the main laboratory is safe to enter again. All measurement systems are shut down:

- ignitrons: the ignitrons are switched off to increase their lifetime and avoid misfires,
- nitrogen: the sample chamber is flushed with nitrogen through a water filter to get rid of any material particles inside,
- data: the data are saved on the measurement computers for further evaluation,
- sample holder: the complete sample holder is removed, cleaned and the windows are exchanged with new ones. Then the outer part is installed again, the correct positioning is important: the incident laser beam should be reflected back by the BK-7 window,
- infrared lamps: after about five minutes, the infrared lamps should turn back on.

With the outer part of the sample chamber installed again, the experiment itself is over and this routine can be performed repeatedly for different samples.

If all experiments are performed, the aperture is switched off:

- infrared lamps: the voltage supply of the infrared lamps is switched off,
- nitrogen: the valves on the nitrogen tank are closed,
- measurement computers: the data are transferred for further analysis and the measurement computers are switched off,
- covers: all optical apertures are covered over night to prevent any collection of dust.

The experimental data are copied from the measurement computers to external storage media for further evaluation. The evaluation is performed with the Matlab program *Hotwire.m*, described in detail by 2000, *Sachsenhofer* [26]. The device matrix needs to be in the *Hotwire* folder to account for all optical components in order to calculate the Stokes vector from the intensities according to Equation 3.8. The device matrix has to be named *Auto_cal.dat* for the Matlab routine to work. After starting the Matlab function, a pop up window opens and the following steps are performed:

- read-in: to read-in the experimental data, the option *Open DOAP - file* should be used if measurements with the DOAP were performed. The measurement file with a file name extension *.raw* is selected. If all other measurement files from the same measurement are named exactly the same, with different file name extensions and if they are in the same folder, they are automatically imported as well,
- evaluation: in the category *Evaluation*, the button *Parameter* can be found. Here all parameters concerning the material are set. This includes the density and most importantly the radiance melting temperature,
- pyrometer: in the category *Evaluation*, the pyrometer used is selected. First only the correct wavelength has to be chosen,
- temperature: the temperature - time dependence is calculated after the *Temperature via melting plateau* routine is used. This routine calculates the calibration factor K from Equation 3.2, which is then manually entered in the category *Pyrometer* from the point above,

- voltage correction: to save the evaluated data, an *Automatic voltage correction* has to be performed, even if the voltage across the wire was not measured.

Three different files are saved with this routine. The most important one being the **.dat* file. This file contains all corrected measurement values and all calculated values during the evaluation. The **.log* and the **.xml* file contain important information about the evaluation and the measurement.

4.5 Good practice

In this chapter first results are presented, which suggest a certain procedure before and during the experiments. Most importantly this contains different handling techniques of the apparatus but also tips for the evaluation. Finally a long term measurement is presented, which describes deviations over several days.

4.5.1 PSD Cover Opening

During calibration, experiments were performed while varying the opening of the cover in front of the PSD. In Figure 4.3 the x-axis shows the entries of the device matrix and the y-axis shows the corresponding values of the device matrix. Each bar represents three measurements with a mean value and the standard deviation. Although the standard deviation already uses an amplification factor of $k = 2$, the error bars are almost not visible since the highest uncertainty is about 0.009, which is slightly over 2 %. For the smallest three aperture diameters, a part of the laser was cut off and only the remaining part of the laser beam was able to reach the detector. According to Figure 4.3 this results in lower values for the entries in the device matrix. At bigger opening angles of the cover, the device matrix seems to stabilize and remain fairly constant at their respective values.

Although the difference of the single device matrix entries looks significant in Figure 4.3, evaluations of a BK-7 measurement with the different device matrices yield a normal spectral emissivity $\epsilon_{\lambda,n} = 0.950 \pm 0.003$ with an

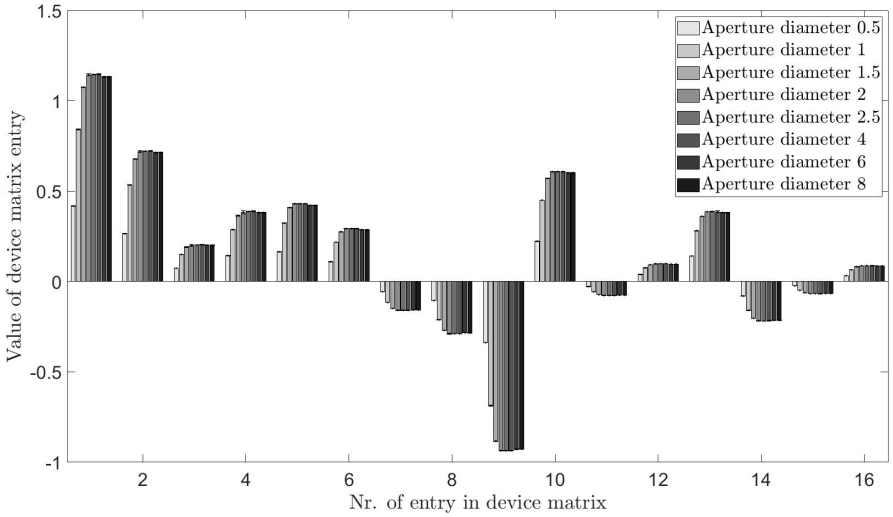

Figure 4.3: Bar graph of the device matrix with varied aperture diameter of the PSD (opening diameter according to the mounted scale), 3 measurements per diameter, error bars from standard deviation with expansion factor of k = 2.

expansion factor of $k = 2$. According to 2001 *Seifter* [8], the theoretical value of the normal spectral emissivity is $\epsilon_{684.5\,\mathrm{nm}} = 0.958$.

In summary the aperture opening, effects the entries of the device matrix quite significantly but the normal spectral emissivity is almost not effected. Although the normal spectral emissivity is almost not effected, the cover was opened at a nominal diameter of 6 on the scale during all further experiments.

4.5.2 Laser Intensity over Time

After the laser was switched on, many calibration experiments were performed over time with the goal of measuring the total intensity of the laser over time. The results are shown in Figure 4.4. A clear trend is observed for the mean intensity but also for the maximum and the minimum intensity over time. During the first 60 minutes, the intensity rises significantly but

also afterwards the intensity shows an increasing trend until about 250 minutes, so slightly over four hours.

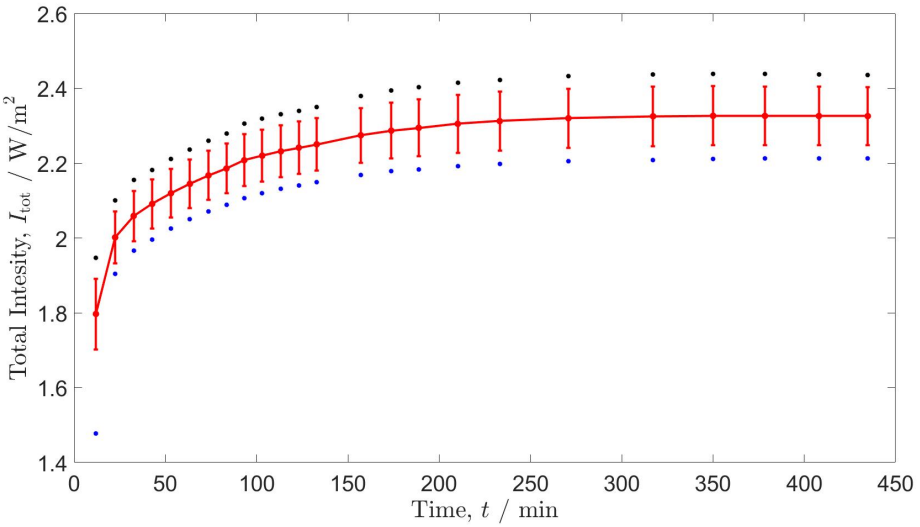

Figure 4.4: Graph of intensity of the laser over time after switching on, measurements performed during calibration without any sample, red line: mean intensity with standard deviation, black dots: maximum intensity during one measurement, blue dots: minimum intensity during one measurement.

Interestingly the deviation of the intensities did almost not change over time. Only during the first experiment a very high deviation was experienced, specifically towards lower intensities. This can be explained by the fact, that the intensity increased between the single measurements for a single polarization and therefore each measurement yields a different total intensity and the whole calibration measurement shows a higher deviation.

Because of the very slow increase and the long time frames, it is assumed, that the laser is warming up slowly until it reaches a constant temperature and light production and therefore the intensity reaches its maximum.

In Figure 4.5, the entries of the device matrix are shown. It shows the same trend as Figure 4.4. In the first 60 minutes, a very strong change can be seen. Afterwards the entries seem to converge towards a stable value. The stable value is reached again after about four hours.

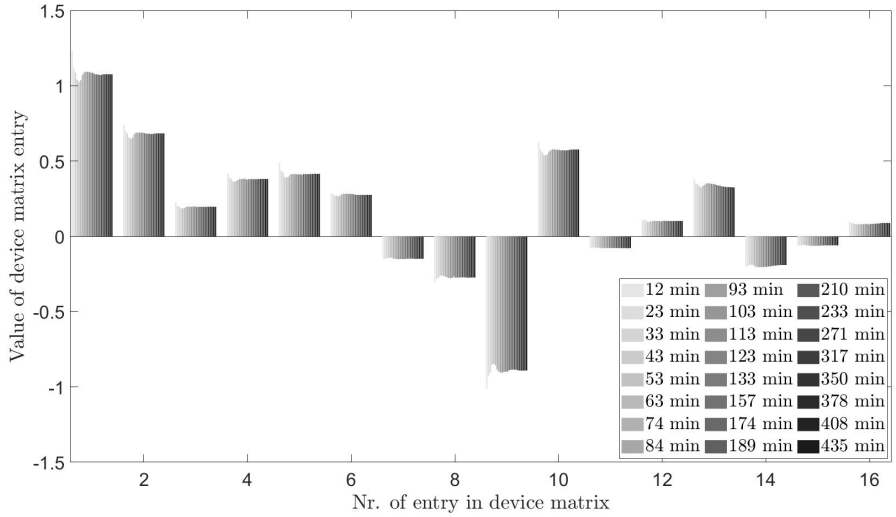

Figure 4.5: Bar graph of device matrix elements over time after switching on the laser, measurements performed during calibration without any sample.

To achieve a constant intensity during the experiments, the laser should be switched on for at least four hours, optimally about five hours, before performing any experiments. For all experiments, performed during this thesis, which require the laser, the laser was switched on at least four and a half hours but for the most part five hours before any measurements were performed.

4.5.3 Long Term Analysis

Single parts of the apparatus used, might move with respect to each other over time. Therefore, it is necessary to account for that and check the position of every single optical component before every experiment. At the start of an experimental day, all spirit levels have to be checked and if necessary the components are adjusted.

Before each experiment, the optical components are positioned and adjusted according to the position of the wire. On the other hand, there are certain parameters that are set during calibration and never changed afterwards.

The angle, at which the PSD is aimed on the wire, is empirically the most important one. But also the positioning of the mirrors, which direct the laser towards the wire, is essential. To ensure the correct position of all optical components, they have to be checked from time to time. From a practical standpoint, it is necessary to minimize the contact to all optical components to avoid any kind of dislocation movement.

Some parameters are easier to check then others. The position of the mirrors can be verified simply by checking the direction of the laser through all optical components. As soon as the laser is not directed centrally through all optical components, the mirrors have to be adjusted. The opposite side of the spectrum is the angle of the PSD. The angle cannot be checked at all with an attached sample chamber. Therefore, it is necessary to adjust the angle during calibration very precisely and check potential change of the angle over a couple of days.

During the calibration for this thesis, calibration measurements were performed over a timespan of almost two weeks and the optical components were adjusted several times. The entries of the device matrix are shown in Figure 4.6. A small deviation between the device matrices, measured on different days, is visible.

There are many reasons, why the device matrix changes over time. The biggest problem is any kind of mechanical movement. This should be avoided at all cost because especially the angle of the PSD needs to be constant at 140° during the measurements.

External influences such as the temperature or humidity can influence the coated beam splitter and the interference filter. This can cause deviation in the device matrix due to a change in the optical components. However, also the electronic components experience a drift, which can differ for the different channels, resulting in a different device matrix. [8]

4.5.4 Melting Plateau Evaluation

During the evaluation, a manual *Temperature via melting plateau* routine is used in order to determine the calibration constant K. Therefore, a hori-

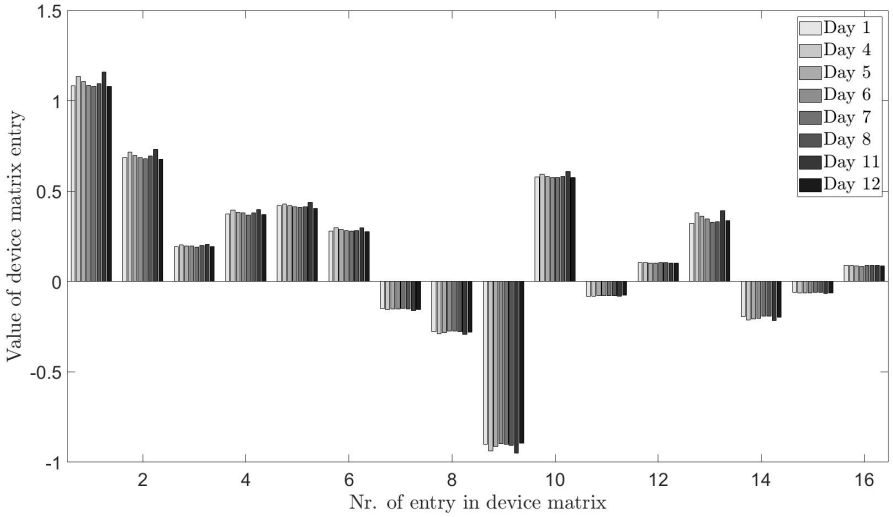

Figure 4.6: Bar graph of the device matrix over time. Every measurement was performed at the same time of the day, with the same intensity of the laser but on different days.

zontal line is dragged directly onto the melting plateau. Together with the previously defined radiance temperature during the melting process, the deviation is calculated and summarized inside the calibration constant.

The quality of the melting plateau differs a lot between different materials but also slight differences between single experiments can be found. The radiance temperature - time dependence is the foundation for all temperature dependent values. Experimentally, everything is measured as a function of time. With the time - radiance temperature dependence, the temperature dependence of all other physical properties can be determined.

Considering the importance of the calibration constant, it is necessary to place the horizontal line, marking the melting plateau, precisely on the same position for experiments of the same material.

In Figure 4.7, two exemplary melting plateaus are shown. Subfigure 4.7a shows the radiance temperature - time dependence of a single molybdenum measurement and subfigure 4.7b depicts the radiance temperature - time dependence of a single tungsten measurement. Even at first glance the shape

of both melting plateaus is very different. In this case, molybdenum shows a typical melting plateau with an almost constant, slightly rising, temperature during the melting process. On the other hand the single tungsten measurement shows a slightly u-shaped melting plateau. One possible explanation for this behaviour is, that the sample is slightly overheated because of the very fast heating process and this means, that the melting process starts slightly delayed.

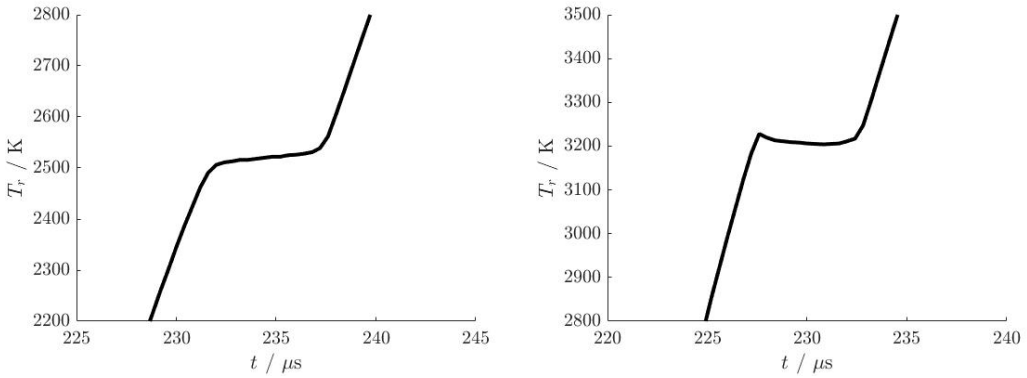

(a) Exampled radiance temperature T_r - time t dependence of a molybdenum measurement.

(b) Exampled radiance temperature T_r - time t dependence of a tungsten measurement.

Figure 4.7: Comparison between two different melting plateau behaviours.

Overall it is important to place the melting plateau at the same position for every experiment for one material. Otherwise a shift of physical properties as a function of the radiance temperature is created. In the case of a similar melting plateau to Figure 4.7a, the horizontal line could either be placed somewhere at the beginning or approximately in the centre of the plateau. If the meting plateau is u-shaped, the horizontal line should be placed somewhere in the centre of the plateau during evaluation, for example at the lowest point within the plateau.

4.6 Useful Tips

Straightening of the wire: depending on the type of material used for the experiments, the wire can be very hard to get completely straight. Especially

tungsten but also molybdenum are challenging materials in this regard. If the wire has kinks or is not straight, movement or instabilities during the heating process can influence the results. Therefore, additional straightening steps were performed in order to straighten the wire as good as possible. Especially the material tungsten was quite challenging. In order to get reasonable results the wire was hung from the ceiling with weights attached over several days. In the end, the wire was even heated up to red heat with a weight attached to get it completely straight.

Positioning of the DOAP: while aligning the DOAP to the wire, looking at the degree of polarization allows a good understanding of the positioning. The degree of polarization should be equal to one, if all systems are adjusted accordingly. To adjust the DOAP, first the reflected intensity is maximized using the PSG and then the PSD is positioned accordingly. For the positioning of the PSD, the degree of polarization can be used to determine the correct position under the condition, that a high enough intensity is detected.

Infrared lamps: during the alignment of the PSG, it is helpful, to close the cover of the PSD completely to maximize the intensity of the reflection. Because the infrared lamps, used to heat up the mercury bath, emit also red light, the reflection of the laser might not be clearly visible. Therefore, the infrared lamps can be switched off temporarily, to allow an easier adjustment of the measurement devices.

Neutral density filter: in front of the pyrometer, a neutral density filter can be installed to lower the intensity of the emitted radiation equally. This allows the measurement of higher temperatures without reaching saturation. This is especially relevant for materials with a high melting temperature. The type of neutral density filter used is material dependent. However, it is important to choose the filter characteristic correctly in order to measure values in the solid phase and the liquid phase as well. This is often only achieved with trial and error. During this thesis, the goal was to achieve about 500°C worth in data points for both phases. This made a linear regression evaluation possible with enough data points in both phases.

5 Measurements

This chapter presents the experimental results of four different pure metals. Specifically the normal spectral emissivity in the solid and the liquid phase will be examined in detail. It was measured with the photopolarimeter, described in Chapter 3.4. Multiple experiments were performed for niobium (Nb), tantalum (Ta), molybdenum (Mo) and tungsten (W) to determine the normal spectral emissivity at 684.5 nm[1]. For the latter two materials, two different samples were used, to confirm the measurement data and compare the data to previous experiments. The results are presented as a function of the radiance temperature[2] of the material, measured with a pyrometer operating at a wavelength of 649.7 nm with a full width at half maximum of 37.2 nm.

To determine the measured normal spectral emissivity at 684.5 nm for one phase, a linear regression line was used to estimate the trend. This is important because the measured data have spikes, which are mostly single measurement points, which do not follow the trend. The linear regression line has the structure of Equation 5.1. $\frac{d\epsilon}{dT_\mathrm{r}}$ describes the slope, therefore the gradient of the normal spectral emissivity with respect to the radiance temperature. ϵ_0 gives the offset of the linear regression line.

Then the linear regression line is extrapolated to the melting radiance temperature to get the normal spectral emissivity at that temperature.

$$\epsilon = \frac{d\epsilon}{dT_\mathrm{r}} \cdot T_\mathrm{r} + \epsilon_0 \tag{5.1}$$

[1] Unless not stated otherwise, any time an emissivity ϵ is mentioned in this chapter, it describes the normal spectral emissivity at 684.5 nm.

[2] Any time a temperature is mentioned in this chapter, it describes the radiance temperature, measured with the 649.7 nm pyrometer.

Such a linear regression line is fitted for both, the liquid and the solid phase. The normal spectral emissivity in the solid phase is highly dependent on the surface preparation before the experiments. Especially the number of applications and the grade of the abrasive paper can make a big difference: the smoother the surface, the lower the emissivity.

The biggest problem with this type of sample preparation is the reproducibility. The experimenter applies the abrasive paper at his own discretion, which results in a slightly different surface for every sample. The homogeneity is another difficult hurdle. As described in Chapter 4.3.1, the abrasive paper was applied, then the wire was turned for about 45° and this procedure was repeated eight or 16 times. This means that it is possible, that the abrasive paper was not applied on every part of the sample equally, resulting in a different normal spectral emissivity on different parts of the wire.

The results are presented with two different uncertainties. The first uncertainty is originating from the statistical distribution of the different experiments. The linear regression lines are given with the two fitting parameters and their respective uncertainties.

Because of spiking, as visible for example in Figure 5.12, the uncertainty can sometimes be very high, up to 50 %. Single measurement points are not following the trend and they can exhibit very high or very low values. However, this is not of prime interest for an average value of the normal spectral emissivity. Therefore, every single experiment is averaged by calculating a linear regression line. Afterwards, the linear regression lines are averaged again, receiving a linear regression line for all measurements. From the single regression lines, the standard deviation is calculated as a first uncertainty estimate. This standard deviation is then used for further calculations, for example the normal spectral emissivity at the melting temperature.

The uncertainty of the normal spectral emissivity at the melting temperature is calculated from the statistical uncertainty, as described above. Additionally, a detailed approach, according to the *Guide to the expression of uncertainty in measurement* (GUM) [2], is used, to quantify different dependences of the device matrix and therefore on the measured intensities. A more detailed description of the uncertainty calculation can be found in Chapter 6. Throughout this chapter, all uncertainties are given in single standard deviations.

5.1 Materials

In this chapter all materials measured are presented together with their relevant properties. For both, tungsten and molybdenum, two different wires were used to compare the results. In both cases no significant deviation was found. For molybdenum, the main reason for a second wire was to check the results with a material used in previous research [21], released also in several publication, for example 2004, *Cagran et al.* [1], 2005, *Cagran et al.* [27] and 2013, *Pottlacher et al.* [19]. The new results are not matching the previously obtained values of the normal spectral emissivity. In the case of tungsten, a second wire was used because the roll-up diameter for storage of the original wire, was too small. Presumably, this resulted in movement of the wire during the experiments due to instabilities in the wire, created during the straightening process. This then resulted in invalid measurements.

In Table 5.1, all metals used, together with their melting radiance temperature $T_{\mathrm{r@650nm}}$ at 650 nm, their melting temperature T_{m} and their density ρ, are summarized. Although the real melting temperature is not used during the evaluation, it is presented to provide context.

Table 5.1: List of all different metals used, together with their relevant properties, $T_{\mathrm{r@650nm}}$ ... melting radiance temperature at 650 nm, T_{m} ... melting temperature, ρ ... density.

Material	$T_{\mathrm{r@650nm}}$ / K		T_{m} / K		ρ / 10^3 kg/m^3
Ta	2820	[19]	3270	[28]	16.65
Nb	2422	[19]	2745	[28]	8.57
Mo	2520	[19]	2895	[28]	10.28
W	3207	[19]	3687	[28]	19.25

Table 5.2 lists all specific materials used and their properties. All samples have a diameter of 0.5 mm.

In the following chapters, the current-time dependence, the temperature-time dependence and the normal spectral emissivity are shown. A more detailed analysis will be provided for tantalum as an example. For the other materials the results and material specific curiosities are discussed.

Table 5.2: Table of all samples used with their purity, *d* ... diameter , prep ... preparation, ID ... identification and mfr. ... manufacturer :
Adv. ... Advent Research Materials
GCL ... Goodfellow Cambridge Limited
Pl. ... Plansee.

material -	purity / wt. %	*d* / mm	prep -	ID -	mfr. -
Nb	99.9	0.5	Temper annealed	LS404934 SJP	GCL
Ta	99.9	0.5	Temper annealed	Gi1109	Adv.
Mo	99.95	0.5	Temper annealed	LS526174 LO	GCL
Mo	n/a	0.5	Electropol. Surf.	n/a	Pl.
W	99.95	0.5	Clean	LS526174 LO	GCL
W	99.95	0.5	Clean	LS251909	GCL

5.2 Tantalum

The metal tantalum, short Ta, melts at a radiance temperature of $T_{\mathrm{r@650nm}} = 2820\,\mathrm{K}$ according to 2013, *Pottlacher et al.* [19]. There are slight deviations in the results of the melting temperature, for example 1976, *Cezairliyan et al.* [29] presents a melting temperature of 2846 K at 653 nm. During the analysis, a temperature of 2820 K was chosen because this result is much more recent.

Compared to other high melting point metals, tantalum has a high density with $16\,650\,\mathrm{kg/m^3}$. This density is needed for the evaluation with the *Hotwire* program. Tantalum with a purity of 99.9%, specified by the manufacturer, was used during the measurements. More details can be found in Table 5.2.

The time control settings are shown in Table 5.3. The table represents all experiments, except for one in which the second delay was 10 µs longer. The data acquisition starts immediately after triggering the experiment. After the first delay (time stamp 2), the first ignitron allows the current to run through the wire, starting the experiment. The second delay is therefore the duration of the experiment and afterwards the second ignitron stops the experiment (time stamp 3). After the third delay, the data acquisition is

stopped and the experiment is finished. The capacitor bank was charged up to a voltage of 5.7 kV for all experiments.

Table 5.3: Time control settings for tantalum, as described in Chapter 3. The first row describes the stage of the process, the second row presents the corresponding time settings. Values of the second row in µs.

1-2	2-3	3-4
190	20	25

For tantalum, abrasive paper was applied eight times and afterwards the wire was cleaned four times with acetone. Between every application the wire was turned for about 45° in order to roughen up and clean the surface evenly.

Altogether, nine experiments were conducted for tantalum. All nine experiments yielded usable results, which are presented in the following. Tantalum is an easy to work with material because it is quite soft and the wire can be bent straight without any problems or damage on the wire.

The pyrometer signals of all experiments are presented in Figure 5.1. Only a selected portion of the entire signal is shown because before the selected window, the experiment has not started and afterwards the pyrometer is in saturation and only a constant signal is measured. After about 210 µs the pyrometer starts to detect a temperature radiation. After about 5 µs the melting plateau is reached at a radiance temperature of 2820 K. Then the wire is in the liquid phase and the temperature rises until the pyrometer reaches saturation, plateauing at a constant signal.

In Figure 5.2, the results of the normal spectral emissivity measurements for tantalum are shown. Below temperatures of 2820 K, the solid phase is observed and above the melting temperature, the emissivity of the liquid phase can be seen.

The linear regression line for the normal spectral emissivity of the solid phase is given by

$$\epsilon_{684.5\,\mathrm{nm},s} = (0.743 \pm 0.075) - (4.47 \pm 2.20) \cdot 10^{-5} \cdot T_\mathrm{r} \tag{5.2}$$

for radiance temperatures between 1650 K and 2790 K. This approximation does not reach the melting temperature because in reality the melting does

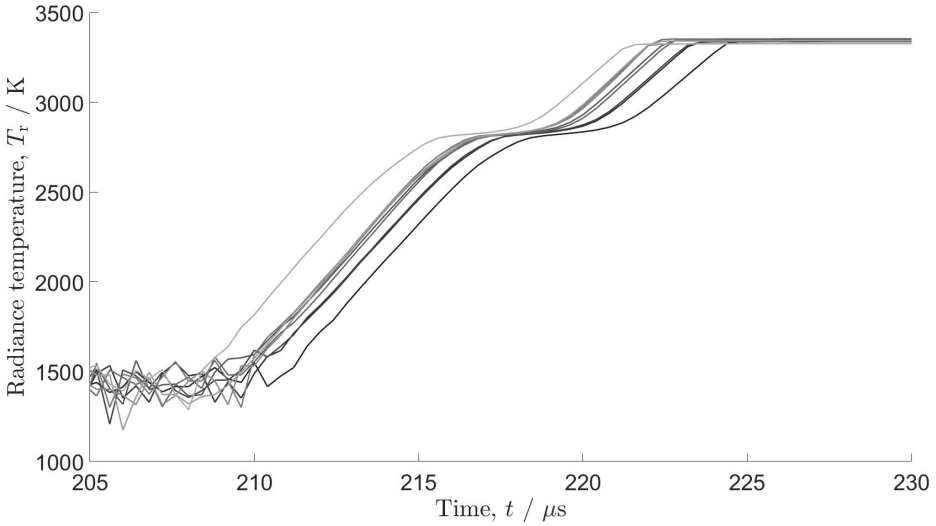

Figure 5.1: Radiance temperatures as a function of time for tantalum (Ta) with a radiance melting temperature of $T_{\mathrm{r@650nm}} = 2820\,\mathrm{K}$.

not happen at exactly one temperature, but during a small temperature interval. The liquid phase can be estimated by the linear regression line

$$\epsilon_{684.5\,\mathrm{nm},l} = (0.573 \pm 0.252) - (6.97 \pm 8.47) \cdot 10^{-5} \cdot T_\mathrm{r} \tag{5.3}$$

for radiance temperatures between 2875 K and 3300 K. By extrapolating this fit towards the melting temperature, the normal spectral emissivity at the melting temperature can be estimated as

$$\epsilon_{684.5\,\mathrm{nm}}(T_\mathrm{m}) = 0.376 \pm 0.027. \tag{5.4}$$

In the liquid phase, close to the melting temperature, the uncertainty is higher than at higher temperatures. This is because not all samples seem to melt under the exact same conditions. Especially one wire shows a slightly different melting pattern compared to all other samples. The emissivity does not seem to drop instantly but exhibits a slower, almost decay-like, melting behaviour.

Looking at the solid phase, one sample stands out because of very high fluctuations. Interestingly, also the average is slightly above the average of

all other samples. Altogether though, the results match up quite nicely with a relatively small uncertainty.

In Figure 5.1, the blue line represents literature values from 2002, *Pottlacher et al.* [30]. The newly measured data are right on the literature value, measured with the same apparatus. According to 2002, *Cagran et al.* [18], the normal spectral emissivity at the melting temperature is equal to 0.366. Also this value, is within the uncertainty interval of Equation 5.4.

Both linear regression lines show a decreasing behaviour towards higher temperatures. This is also in accordance to literature (e.g. [18],[19]).

Moving on towards electronic measurements, Figure 5.3 shows the current through the wire as a function of time. As soon as the first ignitron is triggered, the current starts running through the wire, rapidly increasing in strength. Then the current plateaus and increases slightly in the end, right before the second ignitron is triggered and the current decreases rapidly until no voltage is left on the capacitor bank. As clearly visible in Figure 5.3, one experiment was conducted with slightly different time controls, but no significant deviation is observed in the normal spectral emissivity.

With the time-radiance temperature relation, the current can also be plotted against the radiance temperature, as seen in Figure 5.4. In this figure both phases are again quite distinct and they are separated by a considerable current drop. If the voltage across the wire was measured as well, the current characteristics could be analysed further. For example the ohmic resistance of the wire could be calculated for both phases separately. The offset in current between the different experiments can origin in a different resistance of the sample, for example a slightly longer sample, or it can origin in a different voltage across the wire.

Also the previously observed increase in current, from the current-time relation (Figure 5.3), can be observed in this current-radiance temperature graph, although it is not as distinct. However, a decrease of current in the liquid phase is observed.

Comparing Figure 5.3 to Figure 5.4, it is noticeable, that a time resolved evaluation results in more measurement points at later stages of the experiment. This is caused by the early saturation of the pyrometer, in which all radiance temperature resolved properties enter noise. As described in

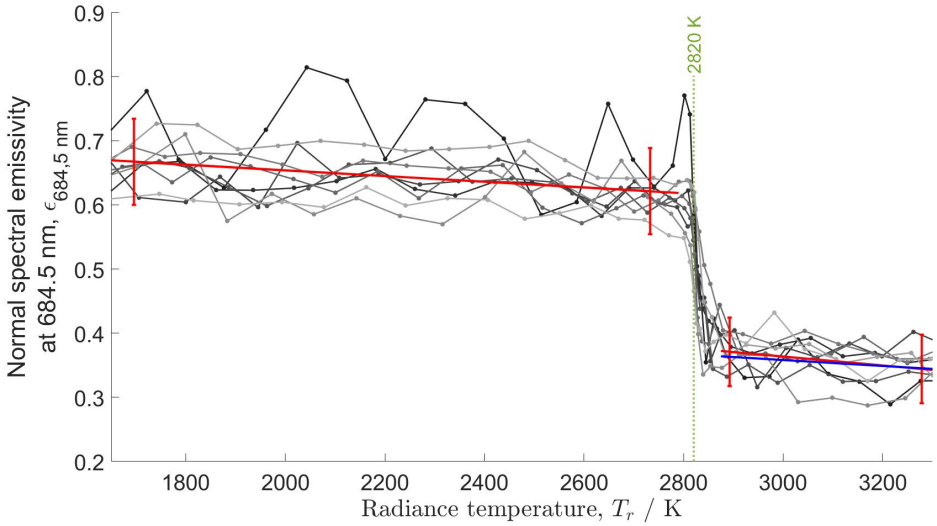

Figure 5.2: Normal spectral emissivity of tantalum (Ta) as a function of radiance temperature, red lines: separate linear regression lines for the solid and the liquid phase with $k = 2$ uncertainties, blue linear line from literature for comparison [30], green dotted line: vertical line to mark the melting temperature of 2820 K [19].

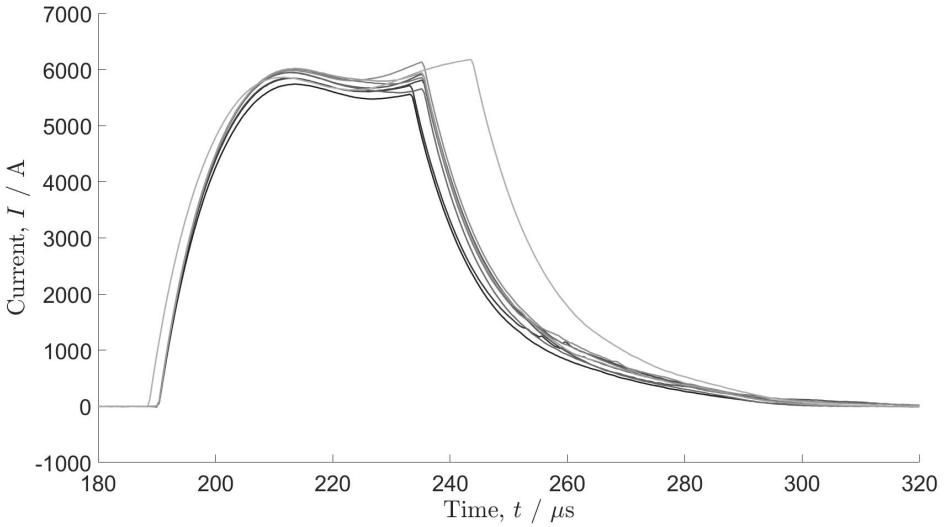

Figure 5.3: Current I through the wire as a function of time t for tantalum (Ta).

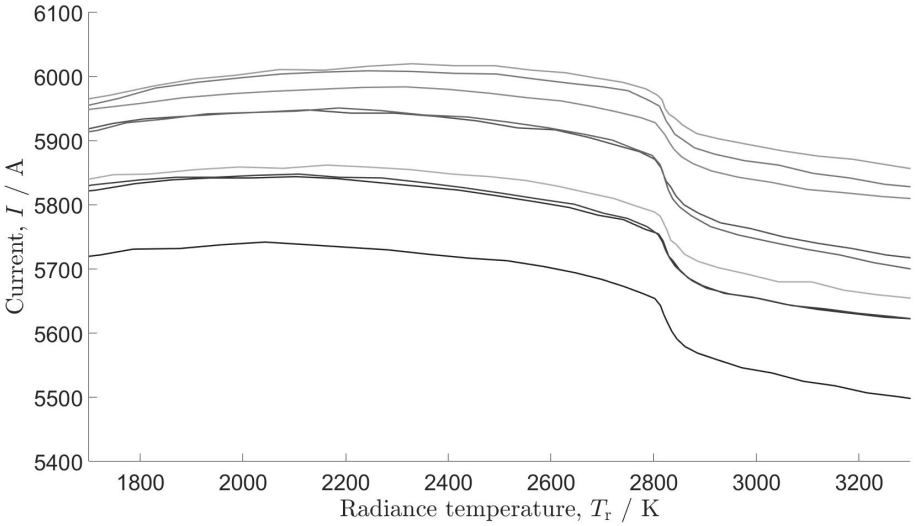

Figure 5.4: Current I through the wire as a function of radiance temperature T_r for tantalum (Ta).

Chapter 4.6, this can be changed easily by using a neutral density filter in front of the pyrometer to lower the intensity equally for all wavelengths.

5.3 Niobium

As second material, niobium was used to determine its normal spectral emissivity. According to 2013, *Pottlacher et al.* [19], the radiance melting temperature at a wavelength of 650 nm is $T_{\mathrm{r@650nm}} = 2422\,\mathrm{K}$. Compared to tantalum, this is a significantly lower melting temperature, which allows more measurement points in the liquid phase without using a neutral density filter.

The density of niobium is with $8570\,\mathrm{kg/m^3}$, only about half of the density if tantalum. The niobium wire used, has a purity of 99.9%, specified by the manufacturer. More details can be found in Table 5.2.

The time control settings are found in Table 5.4. A description can be found in the previous chapter. A voltage of 5.2 kV was charged on the capacitor

bank.

Table 5.4: Time control settings for niobium, as described in Chapter 3. The first row describes the stage of the process, the second row presents the corresponding time settings. Values of the second row in µs.

1-2	2-3	3-4
190	20	30

Similar to tantalum, abrasive paper was applied eight times. Afterwards the wire was cleaned four times with acetone. The wire was turned about 45° between every application of abrasive paper and acetone to ensure an even application.

Altogether, twelve experiments were conducted for niobium. Only ten of those twelve experiments yielded usable results, which are presented in the following. The two missing results exhibit very strong peaks of oscillations in the liquid phase, caused by an abnormal time - temperature dependence. For three of these ten experiments, a neutral density filter was used, allowing measurements at higher radiance temperatures.

Niobium is very easy to work with, because it is quite soft and the wire can be straightened without any problems. This usually allows very easy measurements.

In Figure 5.5, the radiance temperature over time dependence is shown. After about 215 µs, the melting plateau is reached, which lasts for about 5 µs. Afterwards, the liquid phase is reached and at about 3500 K the pyrometer reaches saturation. With the neutral density filter used, the temperature - time dependence is usable up to about 4000 K.

Figure 5.6 shows the normal spectral emissivity measurements of niobium. The linear regression line for the solid phase is given by:

$$\epsilon_{684.5\,\mathrm{nm},s} = (0.664 \pm 0.176) - (2.89 \pm 9.32) \cdot 10^{-5} \cdot T_\mathrm{r} \tag{5.5}$$

for radiance temperature between 1780 K and 2400 K. Again, a slight interval around the melting point is not used for the fitting process because the melting process happens at a small temperature interval and not at a single temperature.

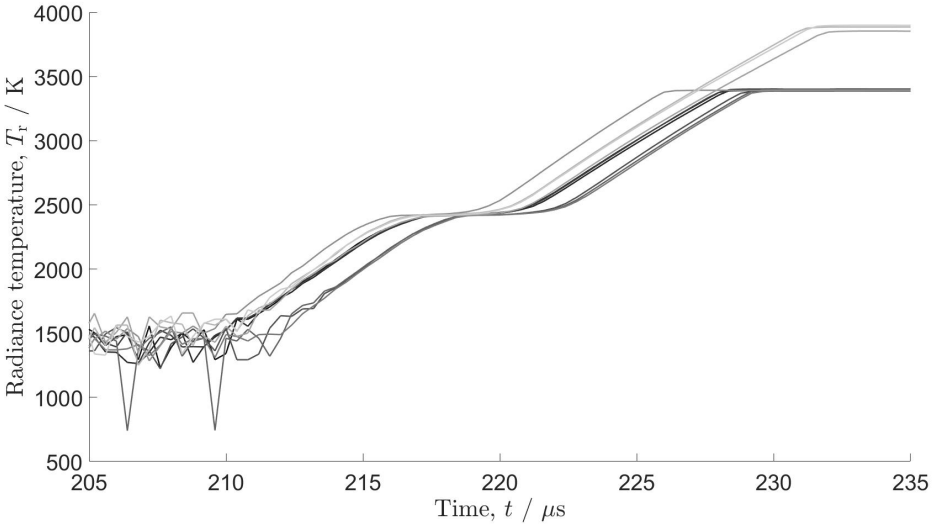

Figure 5.5: Radiance temperatures as a function of time for niobium (Nb), melting temperature T_m =2422 K.

For the liquid phase, the linear regression line is given by:

$$\epsilon_{684.5\,\mathrm{nm},l} = (0.317 \pm 0.189) + (1.15 \pm 5.67) \cdot 10^{-5} \cdot T_r \tag{5.6}$$

for temperature between 2450 K and 3350 K. The linear regression line is extrapolated towards the melting temperature to receive the normal spectral emissivity at the radiance melting temperature

$$\epsilon_{684.5\,\mathrm{nm}}(T_m) = 0.344 \pm 0.060. \tag{5.7}$$

In the solid phase, the measurements are quite spread. Specifically one measurement also exhibits some spikes in the solid phase. Altogether, this results in a much higher uncertainty for the linear regression line compared to tantalum.

But also the liquid phase shows a wider spread and a higher uncertainty than tantalum. Specifically one measurement is at a much higher normal spectral emissivity value that all other. If now all measurements are considered, the linear regression line is spot on the literature value from 2002, *Cagran et al.* [18]. They suggest a constant value in the liquid phase for a

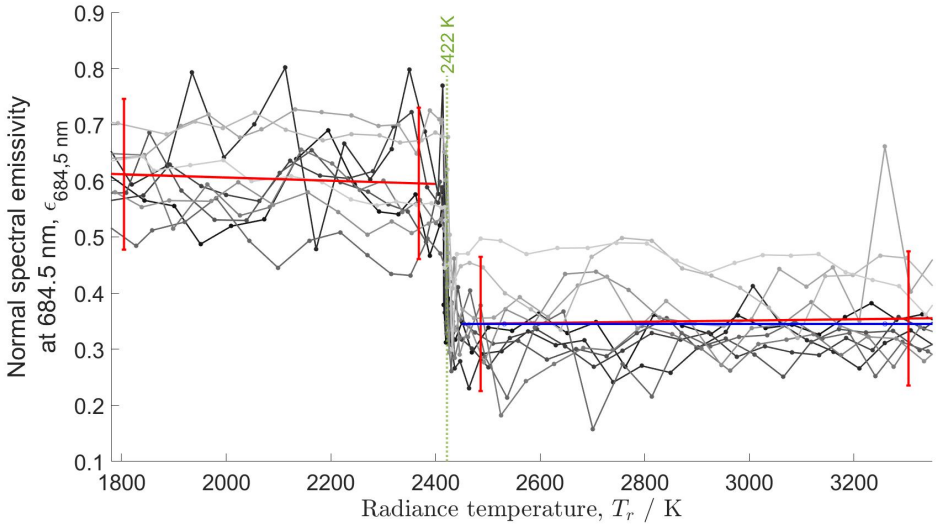

Figure 5.6: Normal spectral emissivity of niobium (Nb) as a function of radiance temperature, red lines: separate linear regression lines for the solid and the liquid phase with $k = 2$ uncertainties, blue linear line from literature for comparison [18], green dotted line: vertical line to mark the melting temperature of 2422 K [19].

pyrometer with a wavelength of 650 nm. The experiments during this thesis suggest a very slight increase towards higher temperatures in the liquid phase but within the uncertainty interval the sign of the slope is insignificant. Their measured value of $\epsilon_{684.5\,nm} = 0.345$ is very close to both the newly measured overall temperature dependent normal spectral emissivity and the newly determined normal spectral emissivity at the melting point.

Figure 5.7 shows the current behaviour over time for the ten different experiments with niobium. A peak current of closely below 6000 A is reached at about 200 µs. Approximately 50 µs after the current starts to flow, the experiment is terminated and the current measured decreases slowly.

To summarize, niobium is typically easy to work with but shows large spikes and a big deviation in the solid and the liquid phase. Averaging all measurement results in a normal spectral emissivity, which is almost perfectly matching literature values.

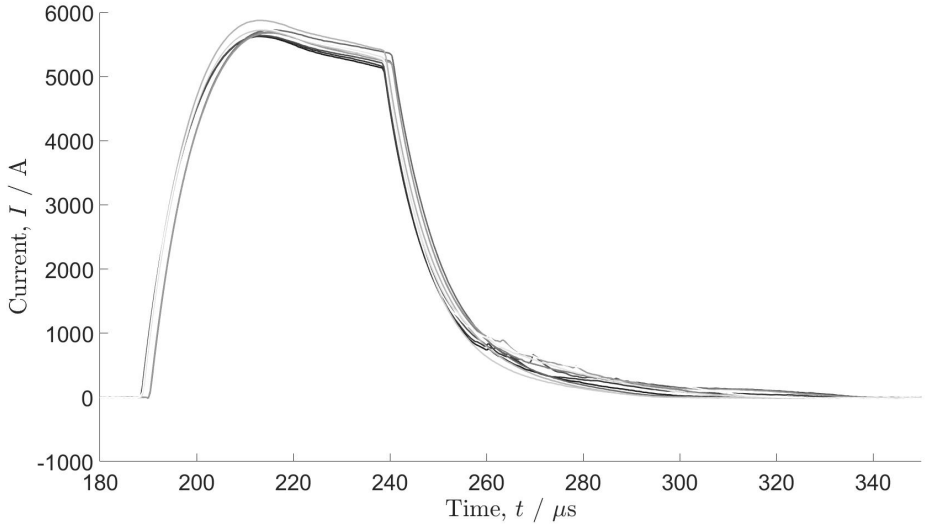

Figure 5.7: Current I through the wire as a function of time t for niobium (Nb).

5.4 Molybdenum

With a radiance melting temperature of 2520 K, according to 2013, *Pottlacher et al.* [19], and a density of 10 280 kg/m^3, molybdenum was used as the third metal for measurements.

The time control settings are listed in Table 5.5. The meaning of the time steps can be found in the previous chapter about tantalum. A voltage of 5.4 kV was charged on the capacitor bank.

Table 5.5: Time control settings for molybdenum, as described in Chapter 3. The first row describes the stage of the process, the second row presents the corresponding time settings. Values of the second row in µs.

1-2	2-3	3-4
190	20	40

Because molybdenum is harder to work with than the previous two metals, abrasive paper was applied more often to roughen up the surface. It was used sixteen times instead of eight. Also acetone was used twice as often as before (eight times).

Molybdenum is more difficult to straighten and that is why more measurements had to be conducted in order to get a reasonable amount of usable results. Altogether, fourteen different experiments were performed and only half of them yielded reasonable results. The other seven experiments, resulted in noise or showed data only in a brief temperature region and outside of that temperature interval the signal was too noisy.

Figure 5.8 shows the radiance temperature development over time. The different experiments are slightly split in time with a deviation of up to 5 µs. The melting process takes about 5 µs, similar to niobium and tantalum.

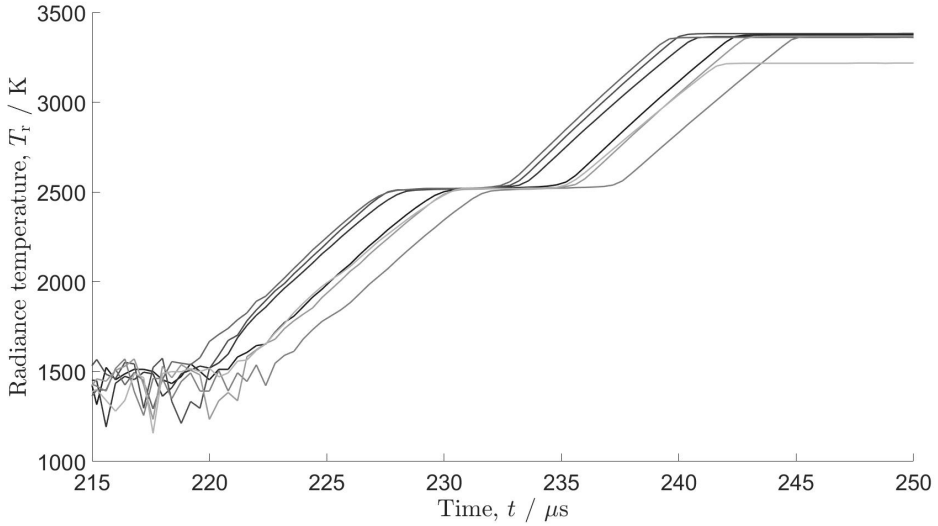

Figure 5.8: Radiance temperatures as a function of time for molybdenum (Mo), melting temperature $T_m = 2520\,K$.

Compared to tantalum or niobium, also the seven usable measurements consist of a lot of peaks and show a very broad band in the liquid phase. Figure 5.9 shows the normal spectral emissivity for the seven experiments with molybdenum.

Looking at the solid phase, two different bands are formed. The difference in normal spectral emissivity is quite significant and there is no overlap. It is also important to mention, that no external reason for this band formation was found. Neither the temperature nor the number of application of the

abrasive paper was different. Also the voltage and the current show no significant difference, which could explain this phenomenon.

To account for the two different bands in the solid phase, three different linear regression lines are used. First, all seven measurements can be approximated with

$$\epsilon_{684.5\,\mathrm{nm},s,all} = (0.623 \pm 0.119) - (6.32 \pm 3.62) \cdot 10^{-5} \cdot T_\mathrm{r} \tag{5.8}$$

for radiance temperature between 1650 K and 2490 K. This radiance temperature interval is also used for both other linear regression lines.

The upper band, denoted with *top*, consists of three different measurements and is given by

$$\epsilon_{684.5\,\mathrm{nm},s,top} = (0.734 \pm 0.086) - (8.36 \pm 4.16) \cdot 10^{-5} \cdot T_\mathrm{r} \tag{5.9}$$

for radiance temperature between 1650 K and 2490 K. The lower band, denoted with *bottom*, consists of four distinct measurements and is given by

$$\epsilon_{684.5\,\mathrm{nm},s,bottom} = (0.540 \pm 0.045) - (4.83 \pm 2.78) \cdot 10^{-5} \cdot T_\mathrm{r} \tag{5.10}$$

for radiance temperature between 1650 K and 2490 K.

The numbers suggest an approximately equal distribution between the two bands of normal spectral emissivity in the solid phase. However, the number of experiments is too low, to reach a conclusion.

In the liquid phase, all seven measurements can be approximated by the linear regression line

$$\epsilon_{684.5\,\mathrm{nm},l} = (0.154 \pm 0.180) - (4.71 \pm 6.30) \cdot 10^{-5} \cdot T_\mathrm{r} \tag{5.11}$$

for radiance temperature between 2550 K and 3190 K. This linear fit can be extrapolated towards the radiance melting temperature of 2520 K to yield the normal spectral emissivity of

$$\epsilon_{684.5\,\mathrm{nm}}(T_\mathrm{m}) = 0.272 \pm 0.028. \tag{5.12}$$

This is significantly lower than the literature value from 2004, *Cagran* [21] and 2004, *Cagran et al.* [1]. The literature development is marked in Figure 5.9 as a blue line. Specifically, at the melting temperature, they suggest a normal spectral emissivity of $\epsilon_{684.5\,\mathrm{nm}}(T_\mathrm{m}) = 0.332$.

This deviation is especially interesting because the experiments were performed with the same apparatus and so far the results were matching previously measured experiments. As a first step towards an explanation, the original molybdenum wire, which yielded the literature results, was used to conduct experiments. This molybdenum wire resulted in comparable values, which are already plotted in Figure 5.9.

Because the original data were measured within the same working group, as next step the original data were found and re-evaluated. This revaluation of the original data from 2004, *Cagran et al.* [1], showed some inconsistencies. Originally seven different experiments were used to determine the normal spectral emissivity.

After carefully looking at the data, one data set was taken out because of an incorrect temperature allocation. This was probably caused by using an incorrect melting temperature during the evaluation, resulting in a completely different melting temperature and values of the solid phase continuing into the liquid phase. With this sample preparation, the solid phase typically exhibits a higher normal spectral emissivity. Therefore, this caused a significant increase in the normal spectral emissivity, especially close to the melting temperature.

Additionally, another data set was omitted because of an atypical course of the emissivity in the liquid phase. According to this measurement, the normal spectral emissivity increases very quickly after melting and starts to oscillate. Furthermore, the signal exhibited a lot of noise, which also made the measurement implausible. Also this data set artificially increased the normal spectral emissivity.

In conclusion, these two data sets both increased the normal spectral emissivity in the liquid phase, especially close to the melting temperature. Once both data sets were removed, an evaluation resulted in significantly different values of the normal spectral emissivity. They confirm the newly measured normal spectral emissivity as they are almost matching.

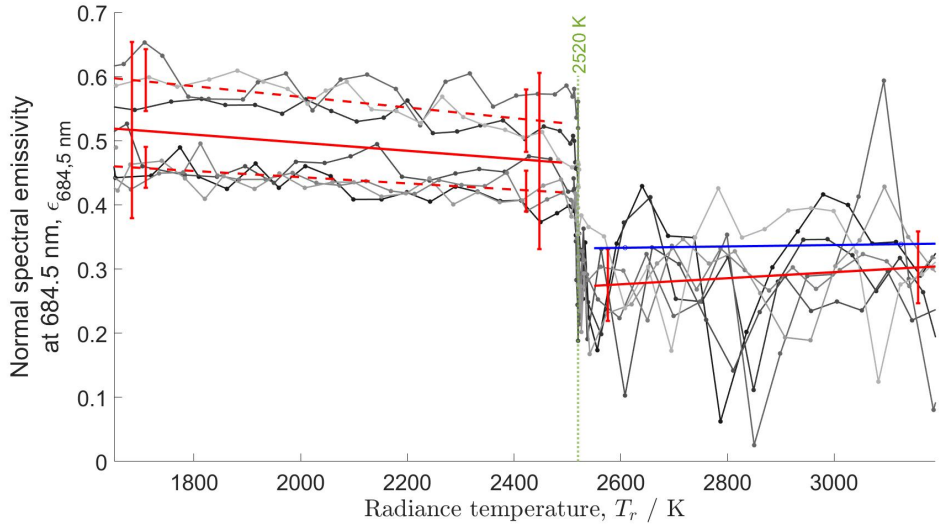

Figure 5.9: Normal spectral emissivity of molybdenum (Mo) as a function of radiance temperature, red lines: separate linear regression lines for the solid and the liquid phase with $k = 2$ uncertainties, blue linear line from 2004, *Cagran et al.* [1], green dotted line: vertical line to mark the melting temperature of 2520 K [19].

Lastly, the current as a function of time is shown in Figure 5.10. Between the single experiments, no significant difference is found. The peak value of the current is slightly higher than a comparable value for niobium or tantalum. The decaying process, after the current is switched off, seems to differ slightly but not drastically.

This deviation seems also not connected in any way with the band formation in the solid phase.

In conclusion, molybdenum is a harder to work with material since is is not that easy to bend and straighten, especially compared to tantalum or niobium. The results for normal spectral emissivity show two bands in the solid phase and a spiking liquid phase. This spiking increases the uncertainty because single values deviate quite drastically from the average.

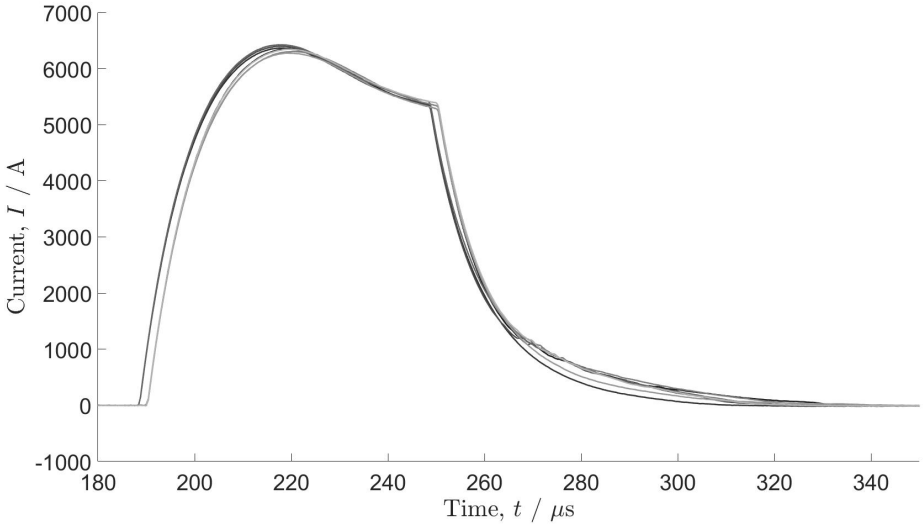

Figure 5.10: Current I through the wire as a function of time t for molybdenum (Mo).

5.5 Tungsten

As the last material, tungsten was used to measure the normal spectral emissivity. With a radiance melting temperature of 3207 K, according to 2013, *Pottlacher et al.* [19], and a density of 19 250 kg/m^3, tungsten is not only the material with the highest melting temperature, out of the four one used, but also has the highest density.

The time control settings are listed in Table 5.6. A description of the time steps can be found in the previous chapter about tantalum. A voltage of 6.1 kV was charged on the capacitor bank.

Table 5.6: Time control settings for tungsten, as described in Chapter 3. The first row describes the stage of the process, the second row presents the corresponding time settings. Values of the second row in µs.

1-2	2-3	3-4
190	30	25

Even compared to molybdenum, tungsten is much harder to work with. Especially the straightening process is very tedious and more than half of

all experiments yielded unusable results. During the sample preparation, abrasive paper was applied more often to roughen up the surface. It was used 16 or even 24 times, instead of eight. Acetone was typically used eight times.

Presumably, there were two different problems occurring for the specific tungsten wire. First of all, the tungsten wire was not annealed. This can cause local instabilities in the wire, which then can cause unevenly distributed voltage drops across the wire, heating up certain areas faster. This then results in movement of the wire and unusable results. Second of all, the diameter, at which the wire was rolled during shipment, was very small. This made the straightening process very difficult and potentially introduced even more local instabilities into the wire.

Out of the first eleven measurements, only one yielded a result, which was not just noise.

As an attempt, to straighten the wire, a 2 m piece was hung from the ceiling with a 15 kg weight attached at the bottom. But even after three days, the progress was not enough. Finally a blowtorch was used to heat up the wire to red heat, as an attempt to anneal the material and at the same time a 5 kg weight was attached at the bottom to straighten the wire. This process was performed in air, which allowed oxidation at the surface. Consequently, the following experiments have to be evaluated with additional caution.

To compensate for that, a different tungsten wire, the second tungsten in Table 5.2, was used for comparison. This specific wire had a much higher roll-up diameter for shipment and experiments yielded usable results more often.

Altogether, one measurement, with the original tungsten wire, without any heating or hanging treatment could be used. Additionally, three experiments with the second tungsten wire and two experiments with the heat treated wire were used for evaluation.

The radiance temperature as a function of time is shown in Figure 5.11. The shape of all curves is very similar, even though three very differently treated wires were used.

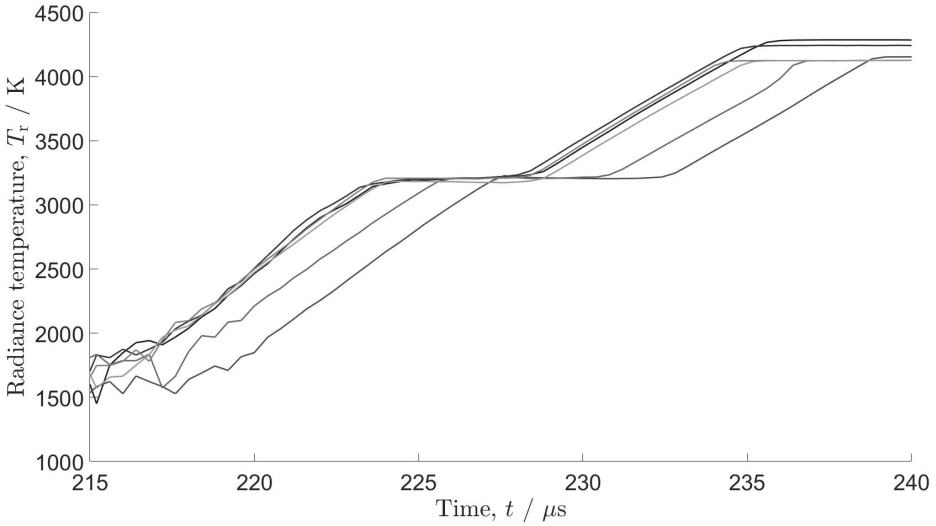

Figure 5.11: Radiance temperatures as a function of time for tungsten (W), melting temperature $T_\mathrm{m} = 3207\,\mathrm{K}$.

All six results of the normal spectral emissivity are shown in Figure 5.12. In the solid phase, all values are in proximity of each other and almost no spiking is observed. The linear regression line for the solid phase is

$$\epsilon_{684.5\,\mathrm{nm},s} = (0.606 \pm 0.119) - (3.68 \pm 5.44) \cdot 10^{-5} \cdot T_\mathrm{r} \tag{5.13}$$

for radiance temperatures between 1950 K and 3180 K. The liquid phase is described by the following linear regression line

$$\epsilon_{684.5\,\mathrm{nm},l} = (0.450 \pm 0.264) - (2.42 \pm 7.03) \cdot 10^{-5} \cdot T_\mathrm{r} \tag{5.14}$$

for temperatures between 3240 K and 4100 K. Analogous to the previous chapters this linear regression line is extrapolated towards the melting temperature to estimate the normal spectral emissivity at the melting point. It is given by

$$\epsilon_{684.5\,\mathrm{nm}}(T_\mathrm{m}) = 0.372 \pm 0.038. \tag{5.15}$$

This value is within the uncertainty interval of literature values. According to 2002, *Cagran et al.* [18], the normal spectral emissivity with a wavelength of 684.5 nm is equal to 0.396.

Looking at the liquid phase, a few very prominent spikes, especially around 3700 K can be observed in both directions. Although the newly measured values are slightly below the literature values, they are still within the uncertainty interval.

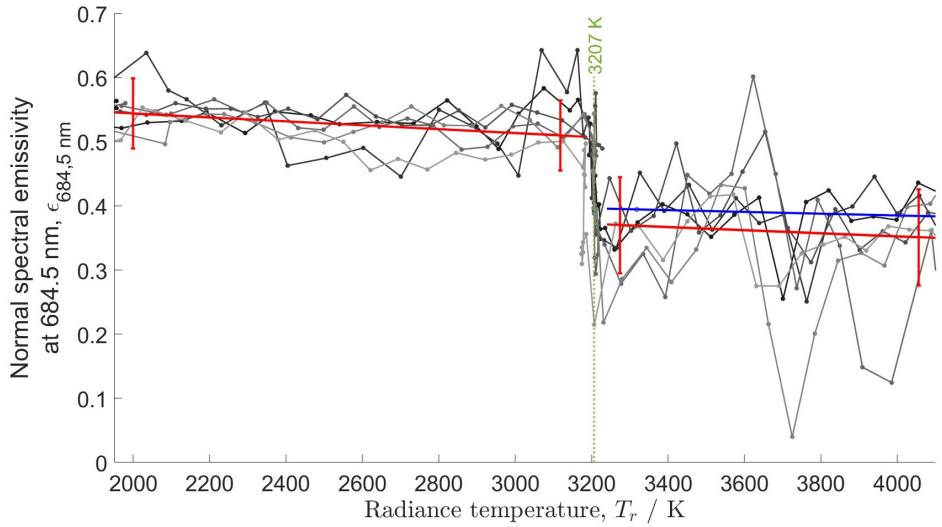

Figure 5.12: Normal spectral emissivity of tungsten (W) as a function of radiance temperature, red lines: separate linear regression lines for the solid and the liquid phase with $k = 2$ uncertainties, blue linear line from literature for comparison 2002, *Cagran et al.*[18], green dotted line: vertical line to mark the melting temperature of 3207 K [19].

Figure 5.13 presents the current behaviour as a function of time for the tungsten measurements. Compared to the previous chapters, in which the current over time dependence depicts only a time delay, here a current deviation is measured. The two slightly lower current curves are both not heat treated. One of them is the single shot of the tungsten wire, which was originally supposed to be measured and the other experiment was performed with the comparison tungsten wire. However, the other two measurements with the comparison tungsten wire are in the upper section, with a slightly increased current flow through the wire. In summary, the current through the wire shows no significant difference between the three different sample types used.

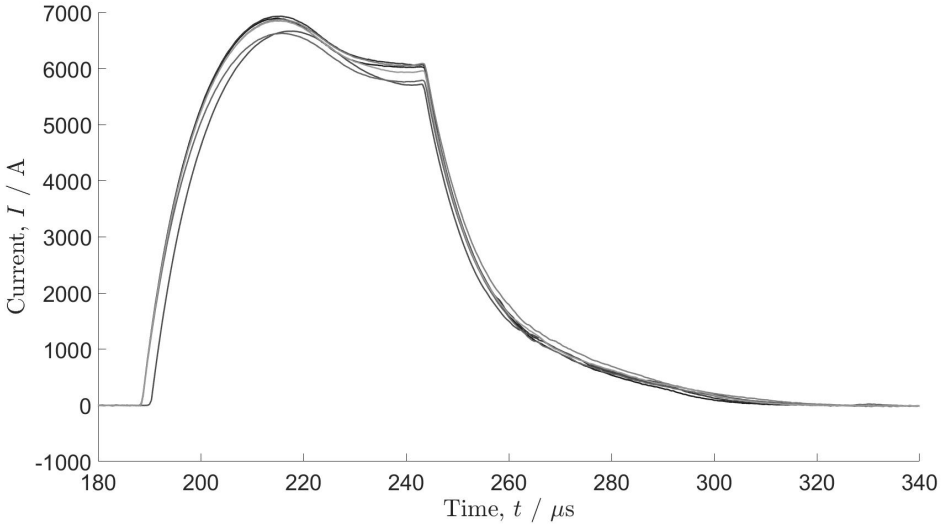

Figure 5.13: Current I through the wire as a function of time t for tungsten (W).

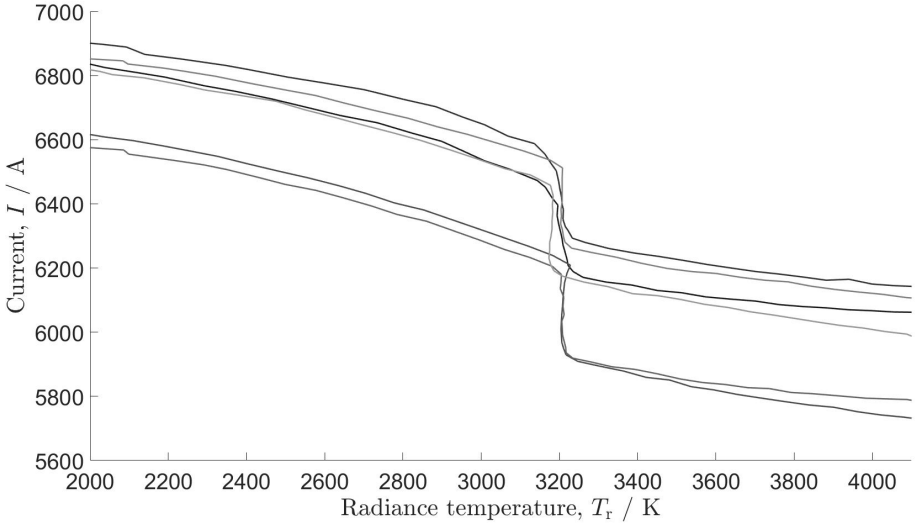

Figure 5.14: Current I through the wire as a function of radiance temperature T_r for tungsten (W).

In addition, Figure 5.14 presents the current as a function of the radiance temperature. A very similar picture compared to Figure 5.13 can be observed.

Two experiments, one from the original wire and one from the comparison wire exhibit a lower current flow during the entire experiment, in both phases.

5.6 Conclusion

In this chapter, the results of four different materials (Ta, Nb, Mo, W) are presented. Details of the materials used can be found in Table 5.2 and Table 5.1. A more detailed analysis, additional figures and a short description of the chosen experimental parameters can be found in the previous chapters.

The summarized linear regression line parameters for the solid phase, of all materials measured, can be found in Table 5.7. All slopes, show a decreasing behaviour towards the melting temperature. The uncertainties of the slopes, for the solid phase, are quite small for tantalum and molybdenum but are even higher than the values for niobium and tungsten. A comparison of the two different linear regression lines of molybdenum shows, that not only the offset but also the slope is different.

However, it has to be kept in mind, that the results of the normal spectral emissivity in the solid phase, depend highly on the surface preparation of the sample.

Table 5.7: Summary of all linear regression line parameters for the solid phase. Parameters according to Equation 5.1.

Material	$\frac{\mathrm{d}\epsilon}{\mathrm{d}T_\mathrm{r}} \cdot 10^{-5}$ / 1/K	$\Delta\frac{\mathrm{d}\epsilon}{\mathrm{d}T_\mathrm{r}} \cdot 10^{-5}$ / 1/K	ϵ_0	$\Delta\epsilon_0$
Ta	-4.47	2.20	0.742	0.075
Nb	-2.89	9.32	0.664	0.176
Mo (top)	-8.36	4.16	0.734	0.086
Mo (bottom)	-4.83	2.78	0.540	0.045
W	-3.68	5.44	0.606	0.119

For the liquid phase, the linear regression line parameters are summarized in Table 5.8 for all materials measured. Here, tantalum, molybdenum and

tungsten exhibit a decrease towards higher temperature but niobium shows a slightly increasing behaviour. Because of spikes in the measurement data, the uncertainties are very high for all linear regression lines.

Table 5.8: Summary of all linear regression line parameters for the liquid phase. Parameters according to Equation 5.1.

Material	$\frac{d\epsilon}{dT_r}$ / 1/K	$\Delta\frac{d\epsilon}{dT_r}$ / 1/K	ϵ_0 in 10^{-5}	$\Delta\epsilon_0$ in 10^{-5}
Ta	-6.97	8.47	0.573	0.252
Nb	1.15	5.67	0.317	0.189
Mo	-4.71	6.30	0.154	0.180
W	-2.42	7.03	0.450	0.264

By extrapolating the linear regression lines back towards the melting temperature, the spectral normal emissivity at the melting temperature can be estimated. The results are summarized in Table 5.9. The uncertainty is, as described in the beginning of this chapter, calculated differently. To eliminate single measurement points, which can sometimes spike, linear regression lines are calculated for every single measurement and then they are averaged, to get a linear regression line of all measurements. Additionally, the standard deviation of these linear regression lines is calculated and used for further uncertainty calculations. Another uncertainty is added quadratically, which considers different experimental parameters, as described in Chapter 6.

Table 5.9: Normal spectral emissivity values ($\epsilon_{684.5\,nm}$) for the radiance melting temperature of all materials, together with their uncertainties ($\Delta\epsilon_{684.5\,nm}$) and literature values ($\epsilon_{684.5\,nm,lit}$).

Material	$\epsilon_{684.5\,nm}$	$\Delta\epsilon_{684.5\,nm}$	$\epsilon_{684.5\,nm,lit}$	
Ta	0.376	0.027	0.366	[18]
Nb	0.344	0.060	0.345	[18]
Mo	0.272	0.028	0.332	[1]
W	0.372	0.038	0.396	[18]

Looking at molybdenum, the resulting normal spectral emissivity at the melting temperature but also throughout the liquid phase, is outside of the

calculated $k = 2$ uncertainty interval. Overall the normal spectral emissivity, in the liquid phase, is lower by about 20 % than literature values from 2004, *Cagran et al.* [1], 2005, *Cagran et al.* [27] and 2013, *Pottlacher et al.* [19].

As described in Chapter 5.4,two data sets of the original data from 2004, *Cagran et al.* [1] were omitted and a new evaluation shows values close to the newly measured normal spectral emissivity. These results were also published in 2020, *Eber et al.* [31].

6 Uncertainty Analysis

This chapter will primarily focus on the evaluation of the uncertainty for the normal spectral emissivity[1]. Unless stated otherwise, all expressions and nominations are in accordance to the *Guide to the expression of uncertainty in measurement* (GUM) [2].

The uncertainty can be traced back to several different causes. It can origin in the apparatus itself or its handling. Most optical components need to be adjusted perfectly, in order to avoid any kind of reflection or loss. A perfect arrangement cannot always be guaranteed and therefore some artificially produced deviations were used to estimate the resulting uncertainty.

The main part of the uncertainty however, origins in the statistical distribution of the results for every measurement. During evaluation an additional uncertainty is introduced because the melting plateau is not a perfect plateau but has a slope. However, a horizontal line is used to mark the melting plateau in order to calculate the calibration constant. In this case a consistent evaluation is the key. Otherwise, a temperature deviation between the different measurements can occur.

Firstly, the influence on the device matrix, Equation 3.21 from 2005, *Wilthan* [5] was used, to calculate the uncertainty budget. However, GUM workbench was not able to calculate the uncertainness. Reevaluation and a manual calculation of the uncertainties with MATLAB, still resulted in in flawed uncertainty values. After careful consideration, the appropriate equations from 2000, *Sachsenhofer* [26] were used and the uncertainty calculation with GUM workbench yielded conclusive results.

[1] Unless not stated otherwise, any time an emissivity ϵ is mentioned in this chapter, it describes the normal spectral emissivity at 684.5 nm.

6.1 Influences on Device Matrix

To calculate the combined uncertainty of all influences, first the uncertainty for every separate influence factor is calculated. For this, the different device matrices were used to evaluate the same calibration measurement of a BK-7 prism.

First of all, the uncertainties of ψ and Δ are calculated from four to five measurements for every influence factor. The variances for all type B uncertainties can be calculated using Equation 6.1.

$$u^2(\Delta) = a^2/3 \tag{6.1}$$

a is half of the distance between the minimal and maximal value. All type B uncertainties are independent of each other, because they origin from different parts of the aperture. Therefore, the combined variance can be calculated via quadratic addition. The uncertainty can then be calculated by applying a square root.

The following four different aspects are considered, while calculating the uncertainty:

Optical cables: Four different optical cables are used to guide the detected light at the PSD towards the measurement cabin for further evaluation. During the experimental preparation, it is possible to touch the insulated optical cables. To consider this possible influence, four different calibration processes were performed, in between which the optical cables were touched, disconnected and even switched. The resulting four different device matrices are shown in Figure 6.1.

Only very small deviations between the different experiments were observed. Δ is given by

$$\Delta = 0.195 \pm 0.044$$

and ψ is given by

$$\psi = 0.351 \pm 0.009.$$

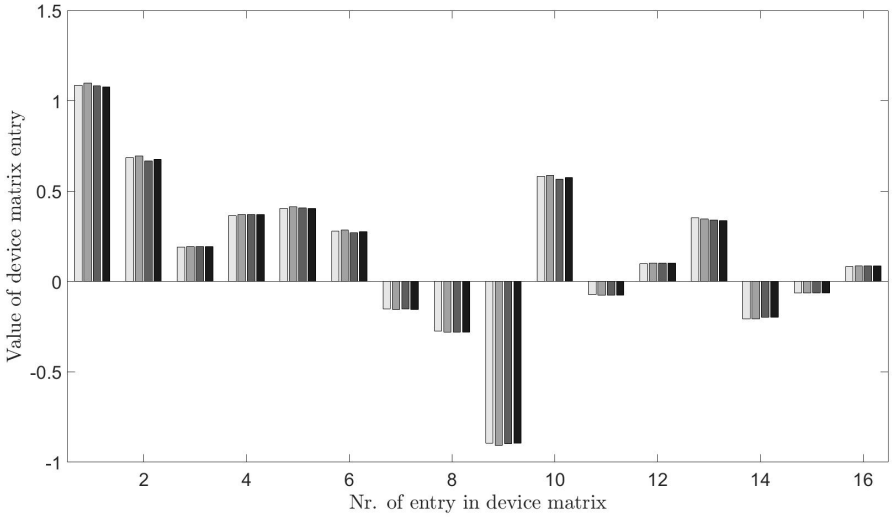

Figure 6.1: Device matrices with intentionally varied, replaced and changed optical cables.

While the uncertainty of Δ is approximately 23 %, the uncertainty of ψ is about 2.5 %. So the uncertainty for the optical cables is almost entirely coming from Δ.

$\lambda/4$ plane: In front on the PSG, a $\lambda/4$ plane is used to counterbalance the linear polarization of the laser light. A perpendicular alignment of the plane to the laser beam is needed, to avoid reflection and resulting losses. To account for any kind of misplacement, the plane was tilted and moved slightly between every single measurement. The results on the device matrix are shown in Figure 6.2.

Δ shows a significant uncertainty and is given by

$$\Delta = 0.122 \pm 0.022,$$

whereas ψ again only exhibits a small uncertainty and is given by

$$\psi = 0.345 \pm 0.002.$$

While the uncertainty of Δ is approximately 18 %, the uncertainty of ψ is below 1 %. Also for the $\lambda/4$ plane, the uncertainty is almost entirely in Δ.

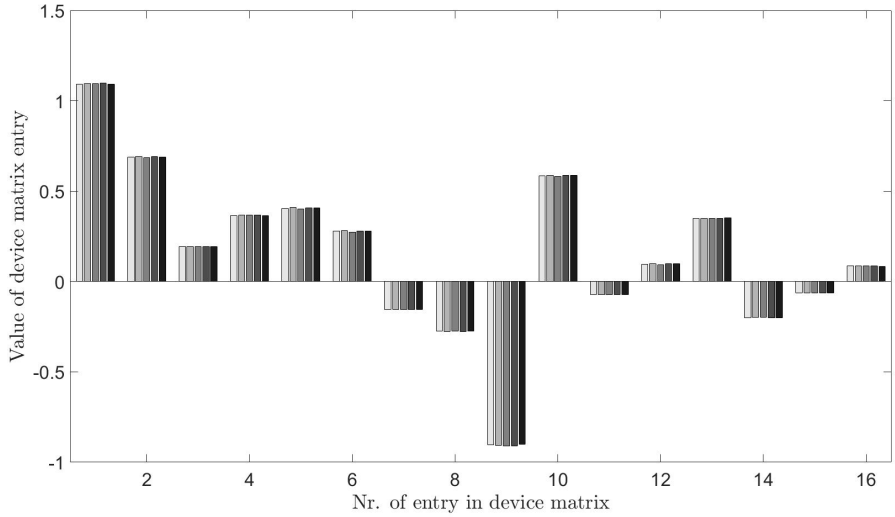

Figure 6.2: Device matrices with intentionally tiled and moved $\lambda/4$ plane.

Reference detector: During the calibration measurements, the reference detector is mounted after the PSG to measure the total intensity. Similar to the $\lambda/4$ plane, a perpendicular alignment with respect to the laser beam is essential. To account for any kind of deviation in the positioning, during the calibration, the reference detector was moved and tilted. The results on the device matrix are shown in Figure 6.3.

Only very small deviations between the different experiments were observed. Δ is given by

$$\Delta = 0.133 \pm 0.026$$

and ψ is given by

$$\psi = 0.346 \pm 0.002.$$

While the uncertainty of Δ is approximately 20 %, the uncertainty of ψ is again below 1 %. Also for the reference detector, the uncertainty is almost entirely in Δ.

Retarder: In front on the PSG, a retarder is used to control the total intensity of the laser beam. A perpendicular alignment of the retarder to the laser

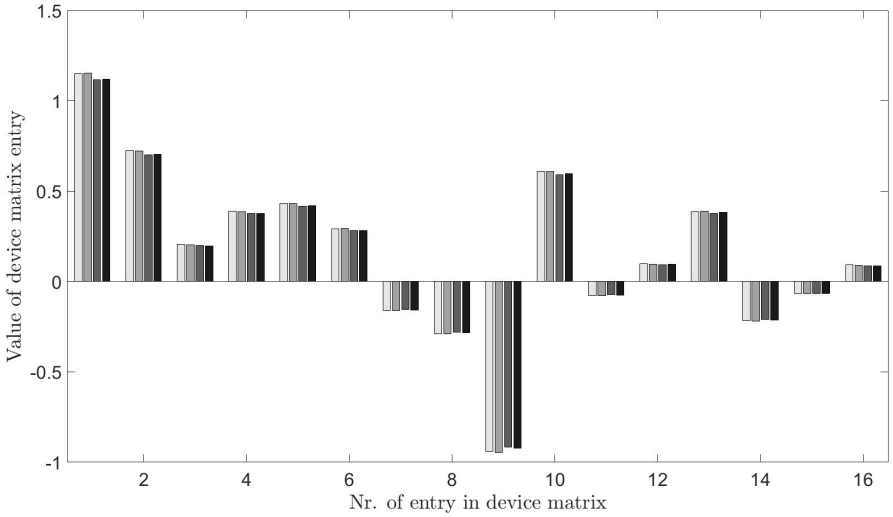

Figure 6.3: Device matrices with intentionally tiled and moved reference detector.

beam is needed, to avoid any kind of reflection or unwanted intensity losses. The procedure, as already used for the previous factors, was executed in between the different experiments, to account for unintentional misplacement. The results on the device matrix are shown in Figure 6.4.

Δ shows a lower uncertainty than before and is given by

$$\Delta = 0.139 \pm 0.010,$$

whereas ψ again exhibits a very small uncertainty and is given by

$$\psi = 0.344 \pm 0.002.$$

While the uncertainty of Δ is approximately 7 %, the uncertainty of ψ is again below 1 %.

In summary, the uncertainty of these four different factors are most dominantly comprised in the uncertainty of Δ. In contrast, the uncertainty of ψ is typically below 3 %.

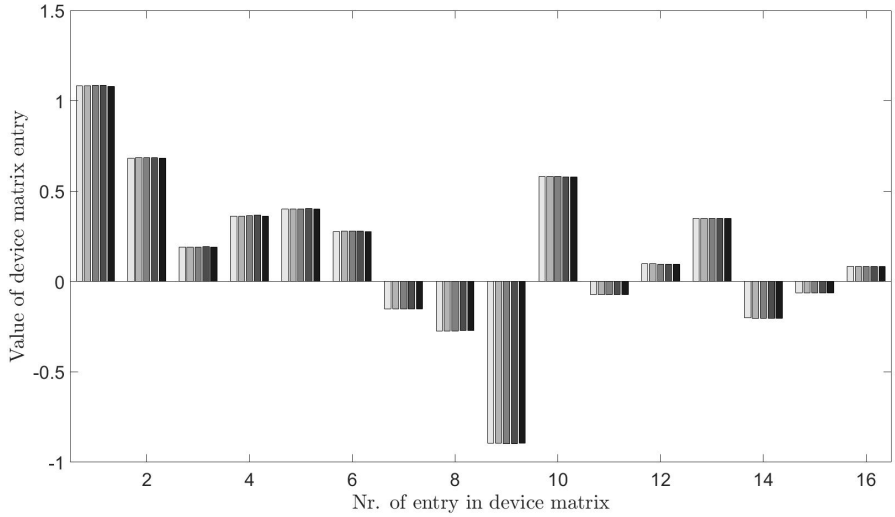

Figure 6.4: Device matrices with intentionally tiled and moved retarder.

By adding the different uncertainties quadratically, the combined uncertainties for Δ and ψ are calculated:

$$u_c(\Delta) = 4.65 \cdot 10^{-2}$$

and

$$u_c(\psi) = 0.63 \cdot 10^{-2}.$$

To consider the correlations between Δ and ψ, the covariance matrix was calculated, using the according MATLAB function. The covariance matrix is given by

$$10^{-3} \cdot \begin{pmatrix} 3.98 & 0.10 \\ 0.10 & 0.02 \end{pmatrix}$$

with a correlation coefficient of 0.35, which suggests a moderate correlation between Δ and ψ. This means all following calculations have to consider this correlation and therefore, the equations for correlated input arguments are used. Equation 6.2 describes the combined uncertainty of a function f.

Table 6.1: Summary of all input parameters for the uncertainty calculation with GUM Workbench.

	x	Δx
n_1	1.0003	
θ	1.220	0.005
ψ	0.3407	0.0036
Δ	0.1792	0.0027

$$u_c = \sum_{i=1}^{2} \left(\frac{df}{dx_i} \right)^2 \cdot u(x_i) + 2 \frac{df}{dx_1} \cdot \frac{df}{dx_2} \cdot u(x_1, x_2) \tag{6.2}$$

Applying Equation 6.2 to the normal spectral emissivity ϵ, the derivations of ϵ, with respect to Δ and ψ, are needed. The first part of the equation represents the uncorrelated uncertainty and the second part requires the covariance matrix for the consideration of the correlation between Δ and ψ. The analytical derivations and the final numerical calculations were performed in GUM Workbench.

At this point, also the uncertainty of the angle of incidence was taken into account. From the experimental set-up, the incidence angle is given by $\theta = 70.0° \pm 0.3°$. The uncertainty is deliberately chosen quite small, because the angle of incidence is adjusted with several different control measurements in order to get as close to 70.0° as possible.

Equation 3.12 to Equation 3.16 are used to calculate the normal spectral emissivity. A derivation of those five equations was performed with respect to Δ, ψ and θ and the uncertainty was calculated separately for a, b, n_2, k_2 and ϵ.

In Table 6.1, the inputs for the calculation of the uncertainty budget with GUM Workbench for the BK-7 measurement are summarized. For the tungsten data point, the values of ψ and Δ are exchanged. The specific values can be found in Table 6.4.

Table 6.2 shows the value and the corresponding uncertainty, with an expansion factor of $k = 2$, for all five parameters for a BK-7 measurement and additionally for a tungsten data point. The resulting uncertainty of the

Table 6.2: Uncertainty budget of all calculated parameters for BK-7 and tungsten (W), uncertainties are provided with an expansion factor of $k = 2$.

	BK-7	W
a	2.32 ± 0.11	-1.82 ± 0.37
b	0.218 ± 0.015	5.37 ± 0.35
n_2	1.529 ± 0.037	2.127 ± 0.071
k_2	0.143 ± 0.008	2.518 ± 0.010
ϵ	0.953 ± 0.005	0.528 ± 0.014

Table 6.3: Uncertainty budget (from GUM Workbench), of BK-7 of the normal spectral emissivity ϵ with the start values, the sensitivity coefficient and the assigned uncertainties to the corresponding parameters.

$x_i \pm u(x_i)$ ... quantity with standard uncertainty (k = 1)
$\frac{\partial \epsilon}{\partial x_i}$ ... sensitivity coefficient
$\frac{\partial \epsilon}{\partial x_i} u(x_i)$ ... standard uncertainty

BK-7	x_i	$u(x_i)$	$\frac{\partial \epsilon}{\partial x_i}$	$\frac{\partial \epsilon}{\partial x_i} u(x_i)$	index
n_1	1.0003				
ψ	0.3470	$3.6 \cdot 10^{-3}$	0.32	$1.2 \cdot 10^{-3}$	21.1 %
Δ	0.1792	$2.7 \cdot 10^{-3}$	-0.037	$-98 \cdot 10^{-6}$	-0.5 %
θ	1.2200	$5 \cdot 10^{-3}$	-0.48	$-2.2 \cdot 10^{-3}$	79.4 %

normal spectral emissivity is given by $\pm$ 0.005 for the BK-7 measurement and $\pm$ 0.014 for the tungsten data point.

Looking at both tables, the uncertainty of the normal spectral emissivity is highly dependant on the angle of incidence. Therefore, it should be adjusted very precisely.

The uncertainty, from the evaluation of tungsten, is added quadratically to the second uncertainty of the normal spectral emissivity from the next chapter in order to estimate the combined uncertainty of the emissivity of a material.

However, this is only an estimation because the uncertainty should be calculated for every single data point. For an accurate result, this extensive calculation would be needed because the uncertainty calculation requires the values of Δ and ψ and not only their uncertainties. Therefore, this specific

Table 6.4: Uncertainty budget (from GUM Workbench), of a tungsten (W) data point of the normal spectral emissivity ϵ with the start values, the sensitivity coefficient and the assigned uncertainties to the corresponding parameters.
$x_i \pm u(x_i)$ ... quantity with standard uncertainty (k = 1)
$\frac{\partial \epsilon}{\partial x_i}$ ... sensitivity coefficient
$\frac{\partial \epsilon}{\partial x_i} u(x_i)$ ... standard uncertainty

W	x_i	$u(x_i)$	$\frac{\partial \epsilon}{\partial x_i}$	$\frac{\partial \epsilon}{\partial x_i} u(x_i)$	index
n_1	1.0003				
ψ	0.4669	$3.6 \cdot 10^{-3}$	-1.0	$-3.8 \cdot 10^{-3}$	30.5 %
Δ	1.8900	$2.7 \cdot 10^{-3}$	-0.23	$-600 \cdot 10^{-6}$	2.3 %
θ	1.2200	$5 \cdot 10^{-3}$	-1.2	$-5.8 \cdot 10^{-3}$	67.2 %

tungsten data point was chosen because it provides the highest uncertainty out of the data points tested. This is only an estimate of the uncertainty. The other data points tested, resulted somewhere between the uncertainties of the BK-7 measurement and the presented tungsten data point.

6.2 Influences at Measurements

Because the experiment yields slightly different results every single time, this deviation is summarized in the standard deviation of the different experiments. To calculate the standard deviation, first a linear regression line was performed for every single measurement in the solid and the liquid phase. By averaging these linear regression lines, a linear approximation of all measurements is calculated. Additionally, the standard deviations for every single point of the single linear regression lines are calculated. This is shown for tantalum in Figure 6.5. The uncertainty bars represent uncertainties at one specific point. The average is then used further as an uncertainty estimated of the normal spectral emissivity at the melting point.

This method accounts for single points, which do not follow the typical trend, but spike. If the first averaging process is omitted, the resulting uncertainty can reach up to 30 % of the measured value. Because the results,

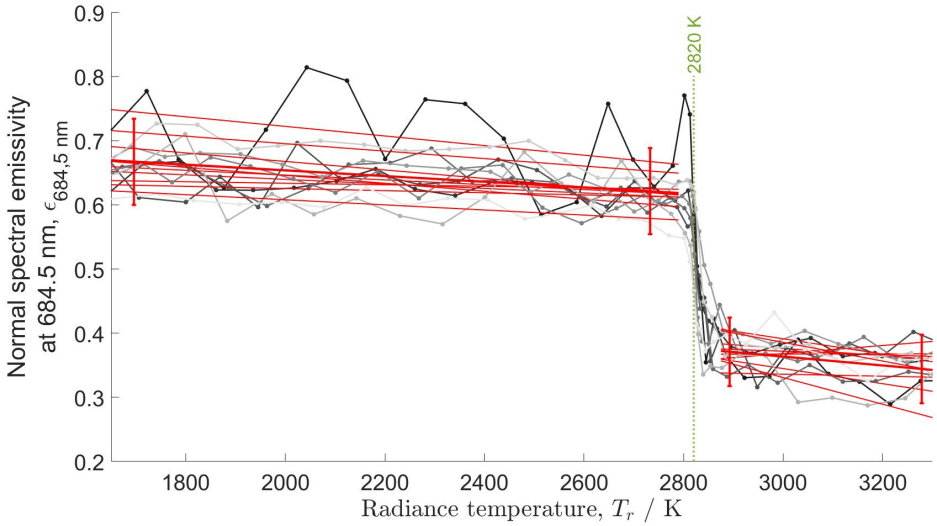

Figure 6.5: Normal spectral emissivity of tantalum (Ta) as a function of radiance temperature, separate linear regression lines for the solid and the liquid phase for every single experiment (thin red lines) and the average (thick red line) to evaluate the standard deviation of the normal spectral emissivity. The green dotted line marks the melting temperature.

using this apparatus, are comparable to other data, this artificially increased uncertainty is compensated by this method of uncertainty calculation.

With this technique, the resulting uncertainty typically is in the range of 10 % of the measured value.

6.3 Influences at Evaluation

During the evaluation, the melting plateau is marked with a horizontal line in order to calculate the calibration constant. Figure 4.7 shows two possible melting plateaus. Depending on the positioning of the horizontal line, used during the evaluation, a displacement of the normal spectral emissivity along the temperature axis takes place. During the evaluations, a temperature displacement of 15 K was observed with intentionally displaced melting plateaus. This mostly depends on the slope of the melting plateau.

However, this uncertainty is insignificant if the melting plateaus are chosen consistently. Because the melting plateaus look very similar for a single material, the horizontal line can either be set centrally, or at either end of the plateau. As long as the line is chosen at the same position, the whole data set has an uncertainty of 15 K.

7 Outlook

During this thesis, it was discovered that the laser has to run for about four to five hours before any experiment can be performed. This observation is described in detail in Chapter 4.5.2. This lead time makes experimenting very time consuming because the number of experiments per day is limited. One possible solution to this problem could be, to add a timer. Prior to any experiments, this timer could switch on the laser, reducing the lead time significantly. This however, would also require switching on the measurement computer and executing a program, which is needed to switch on the laser.

For reliable results in the solid phase, a completely reproducible preparation sequence is needed. Several different parameters need to be controlled precisely during this routine. One possibility could be, to use some kind of sand blaster. This machine could roughen up the surface homogeneously and therefore allow better results in the solid phase.

From an experimental standpoint, the straightening of the wire is one of the major hurdles to receive usable results from the measurement. This is especially challenging, because the roll diameter for shipping is typically very small. An automated way to straighten the wire would come in handy and could increase the yield of usable results. Potentially even the quality of the results could increase because the spiking in the data measured could be reduced.

The high uncertainty, caused by the spiking of single data points, is also a problem that could be addressed in the future. In order to understand the origin of these spikes, a signal analysis is needed and the results could then be checked for irregularities.

Appendix

All measurement data and the evaluation of the four metals can be found online, by using the DOI *10.5281/zenodo.4382073*.

Bibliography

[1] C. Cagran; B. Wilthan and G. Pottlacher. "Normal spectral emissivity at a wavelength of 684.5 nm and thermophysical properties of liquid Molybdenum." In: *International Journal of Thermophysics* 25 (2004), pp. 1551–1566 (cit. on pp. vii, ix, 51, 64, 65, 72, 73).

[2] *Evaluation of measurementdata — Guide to the expressionof uncertainty in measurement*. JCGM. Sept. 2008 (cit. on pp. vii, ix, 50, 75).

[3] *The InternationalSystem of Units (SI)*. 9th ed. Bureau Internationaldes Poids et Mesures. 2019 (cit. on p. xi).

[4] S. English. "Stephan Boltzmann Law and Boltzmann's Constant." Wooster, Ohio 44691; Physics Department, The College of Wooster, Apr. 1999 (cit. on p. xi).

[5] B. Wilthan. "Verhalten des Emissionsgrades und thermophysikalische Daten von Legierungen bis in die flüssige Phase mit einer Unsicherheitsanalyse aller Messgrößen." PhD thesis. Technische Universität Graz, 2005 (cit. on pp. xi, 24, 75).

[6] W. Blanke. *Die Internationale Temperaturskala von 1990: ITS-90*. Physikalisch-Technische Bundensanstalt, 1989 (cit. on pp. 1, 18).

[7] R.M.A. Azzam. "Division-of-amplitude Photopolarimeter (DOAP) for the Simultaneous Measurement of All Four Stokes Parameters of Light." In: *Optica Acta: International Journal of Optics* 29.5 (May 1982), pp. 685–689. DOI: 10.1080/713820903 (cit. on pp. 1, 20).

[8] A. Seifter. "Bestimmung des normalen spektralen Emissionskoeffizienten von flüssigen pulsgeheizten Metallen mittels eines schnellen Photopolarimeters." PhD thesis. Technische Universität Graz, 2001 (cit. on pp. 3, 6, 8, 13, 17–19, 21–26, 30–32, 34, 41, 44).

[9] D. P. DeWitt and Gene D. Nutter. *Theory and practice of Thermal Radiation*. John Wiley & Sons, Ltd, 1989. ISBN: 0471610186 (cit. on pp. 3, 4, 6–8, 10–12).

[10] Dr. Y. Ohno. "Final draft Oct.20, 1999: OSA Handbook of Optics, Volume III Visual Optics and VisionChapter for Photometry and Radiometry." Oct. 1999 (cit. on p. 4).

[11] W. Demtröder. *Experimentalphysik 2, Elektrizität und Optik*. Springer-Verlag Berlin Heidelberg, 2013. DOI: 10.1007/978-3-642-29944-5 (cit. on pp. 6, 7).

[12] NIST. *2006 Radiation Thermometry Short Course*. 2006 (cit. on pp. 8, 9, 11).

[13] Y.S. Touloukian and D.P. DeWitt. *Thermal Radiative Properties: Metallic Elements and Alloys*. Thermal Radiative Properties: Metallic Elements and Alloys Teil 2. Springer US, 1970. ISBN: 9780306670275. URL: https://books.google.at/books?id=9gMpAQAAMAAJ (cit. on pp. 8–10).

[14] S. D. Scopatz et al. "Comparison of emissivity evaluation methods for infrared sources." In: *Infrared Imaging Systems: Design, Analysis, Modeling, and Testing XX*. Ed. by Gerald C. Holst. Vol. 7300. International Society for Optics and Photonics. SPIE, 2009, pp. 256–266. DOI: 10.1117/12.818217. URL: https://doi.org/10.1117/12.818217 (cit. on p. 8).

[15] D. Meschede. *Gerthsen Physik*. Springer-Verlag Berlin Springer-Verlag Berlin Heidelberg, 2010. ISBN: 978-3642128936 (cit. on p. 8).

[16] F.P. Incropera et al. *Fundamentals of Heat and Mass Transfer*. Wiley, 2007. ISBN: 9780471761150. URL: https://books.google.at/books?id=%5C_P9QAAAAMAAJ (cit. on p. 11).

[17] E. Kaschnitz; G. Pottlacher and H. Jaeger. "A new microsecond pulse-heating system to investigate thermophysical properties of solid and liquid metals." In: *International Journal of Thermophysics* 13.4 (July 1992), pp. 699–710. DOI: 10.1007/BF00501950 (cit. on p. 13).

[18] C. Cagran et al. "Liquid-phase behaviour of normal spectral emissivity at 684.5 nm of some selected metals." In: *High Temperatures-High Pressures* 34.6 (2002), pp. 669–679. ISSN: 1472-3441. DOI: 10.1068/htjr067. URL: http:%5C%5Cpdf-file%5C%5C//dx.doi.org/10.1068/htjr067 (cit. on pp. 13, 55, 59, 60, 68, 69, 72).

[19] G. Pottlacher et al. "Normal spectral emissivity near 680 nm at melting and in the liquid phase for 18 metallic elements." In: *TEMPERATURE: ITS MEASUREMENT AND CONTROL IN SCIENCE AND INDUSTRY, VOLUME 8: Proceedings of the Ninth International Temperature Symposium*. Vol. 1552. 1. AIP Publishing. 2013, pp. 704–709 (cit. on pp. 13, 51, 52, 55–57, 60, 61, 65, 66, 69, 73).

[20] M. Leitner et al. "Thermophysical Properties of Liquid Aluminum." In: *Metallurgical and Materials Transactions A* 48.6 (June 2017), pp. 3036–3045. ISSN: 1543-1940. DOI: 10.1007/s11661-017-4053-6. URL: https://doi.org/10.1007/s11661-017-4053-6 (cit. on p. 13).

[21] C. Cagran. "Untersuchung des Emissionsverhaltens flüssiger Metalle mittels Photopolarimetrie und Mehrwellenlängenpyrometrie." PhD thesis. Technische Universität Graz, 2004 (cit. on pp. 13, 19, 25, 26, 51, 64).

[22] E. Kaschnitz. "Bestimmung thermophysikalischer Daten verschiedener Metalle bei ohmscher Pulsheizung im Mikrosekundenbereich." PhD thesis. TU Graz, 1992 (cit. on p. 14).

[23] A. Seifter et al. "Microsecond laser polarimetry for emissivity measurements on liquid metals at high temperatures - application to niobium." In: *International journal of thermophysics* 22.5 (2001), pp. 1537–1547 (cit. on p. 20).

[24] K. K Sharma. *Optics: principles and applications*. eng. Amsterdam; Boston: Academic Press, 2006. ISBN: 1-280-62172-9. URL: https://learning.oreilly.com/library/view/optics/9780123706119/chapter-64.html (cit. on p. 21).

[25] R. M. A. Azzam. "Beam-Splitters for the Division-of-Amplitude Photopolarimeter." In: *Optica Acta* 32 (1985), pp. 1407–1412 (cit. on pp. 22, 26).

[26] F. Sachsenhofer. "Data evaluation for pulse heating experiments combined with emissivity measurements using adivision-of-amplitude photopolarimeter." MA thesis. Institut für Experimentalphysik der Technischen Universität Graz, 2000 (cit. on pp. 23, 39, 75).

[27] C. Cagran et al. "Spectral Emissivitics and Emissivity X-Points of Pure Molybdenum and Tungsten." In: *International Journal of Thermophysics* 26.4 (2005), pp. 1001–1015. DOI: 10.1007/s10765-005-6680-1 (cit. on pp. 51, 73).

[28] R.E. Bedford et al. "Recommended values of temperature on the International Temperature Scale of 1990 for a selected set of secondary reference points." In: *Metrologia* 33 (1996), pp. 133–154 (cit. on p. 51).

[29] A. Cezairliyan et al. "Radiance temperature of tantalum at its melting point." In: *High Temperatures - High Pressures* 8.1 (1976), pp. 103–111. URL: http://inis.iaea.org/search/search.aspx?orig_q=RN:08286409 (cit. on p. 52).

[30] G. Pottlacher and A. Seifter. "Microsecond Laser Polarimetry for Emissivity Measurements on Liquid Metals at High Temperatures - Application to Tantalum." In: *International Journal of Thermophysics* 23 (2002), pp. 1267–1280 (cit. on pp. 55, 56).

[31] A. Eber; P. Pichler and G. Pottlacher. "Re-investigation of the normal spectral emissivity at 684.5 nm of solid and liquid molybdenum." In: *International Journal of Thermophysics* (2020). DOI: 10.1007/s10765-020-02769-7 (cit. on p. 73).